Advances in the Estimation of High Spatio-Temporal Resolution Pan-African Top-Down Biomass Burning Emissions made using Geostationary Fire Radiative Power (FRP) and MAIAC Aerosol Optical Depth (AOD) Data

Authors:

Hannah M. Nguyen[a,c] and Martin J. Wooster[a,b]

a. King's College London, Department of Geography, Aldwych, London WC2B 4BG, UK.

b. National Centre for Earth Observation, (NCEO), King's College London, Aldwych, London WC2B 4BG, UK.

c. Centre for Cross-Disciplinary Approaches to Non-Equilibrium Systems (CANES), King's College London, Strand, London WC2R 2LS, UK.

Corresponding Author: Hannah M. Nguyen, hannah.nguyen@kcl.ac.uk

Abstract

We provide major updates to the ‘top down’ Fire Radiative Energy Emissions’ (FREM) approach to biomass burning emissions calculations, bypassing the estimation of fuel consumption that is a major source of uncertainty in widely used ‘bottom up’ approaches. The FREM approach links satellite observations of fire radiative power (FRP) to emission rates of total particulate matter (TPM) via spatially varying smoke emissions coefficients ($g.MJ^{-1}$) – each derived from matchups of FRP and smoke plume aerosol optical depth (AOD). In the original FREMv1 approach, FRP data came from the geostationary Meteosat satellite and AOD data from the 10 km spatial resolution MODIS MOD04 aerosol product. However, the latter often performs quite poorly close to biomass burning sources due to its large 10 km pixels, bias at high MODIS view zenith angles, and saturation and/or removal of areas of high AOD - limitations introducing bias and uncertainty into the final FREM-derived smoke emissions estimates. We address each of these issues through a series of significant methodological and input data improvements, including exploitation of the 1 km MODIS MAIAC AOD product that performs far better close to fire sources. We use our FREMv2 methodology to generate a new pan-African fire emissions inventory for TPM and the carbonaceous gases CO_2, CO and CH_4, and our annual mean TPM emissions are within 11% of those of the MODIS-based FEER top-down approach, but significantly higher than those of GFASv1.2 and GFEDv4.1s (by 114% and 69% respectively) - agreeing with independent assessments that aerosol emissions of GFASv1.2 require upscaling by a factor of 2 to 3.4 to deliver matching magnitudes between modelled and observed AODs. From our carbonaceous emissions totals we map dry matter consumed (DMC) across Africa, and dividing this by the FireCCISFD11 20 m burned area product we provide one of the first data-driven pan-African maps of fuel consumption per unit area ($kg.m^{-2}$) which in many areas is higher than in GFEDv4.1s. Our estimates represent the highest spatio-temporal resolution biomass burning emissions data yet available over Africa, and strongly advance the aim of a pan-tropical and mid-latitude inventory based on FRP from the global geostationary satellite network (Meteosat, Meteosat IOD, GOES and Himawari).

1. INTRODUCTION

Biomass burning is amongst the largest contributors of gaseous and particulate emissions to the atmosphere, generating a significant fraction of the global atmospheric load of black carbon (BC), particulate matter (PM) and carbon monoxide (CO) (Andreae and Merlet, 2001; Forster et al., 2007; Reddington et al., 2016). Emissions impact regional and global air quality, weather and climate variability (Crutzen and Andreae, 1990; Randerson et al., 2006; Westerling et al., 2006; Schultz et al., 2008; Akagi et al., 2011). The highly dynamic spatio-temporal nature of landscape fires makes their emissions challenging to quantify and satellite Earth Observation (EO) offers the only means to do so over large spatial scales, especially where near real-time information is required. However, despite advancements in the quality of EO data and in fire emission inventory methodologies (Seiler and Crutzen, 1980; Flannigan and Vonder Haar, 1986; Pereira et al., 1999; Justice et al., 2002; Wooster et al., 2005; Van Der Werf et al., 2006; Ichoku et al., 2008; Vermote et al., 2009; Lehsten et al., 2009; Wiedinmyer et al., 2011; Kaiser et al., 2012; Ichoku and Ellison, 2014; Darmenov and da Silva, 2015; Mota and Wooster, 2018), large uncertainties and discrepancies remain between the different inventories.

Most fire emission inventories use a ‘bottom-up’ approach, in which estimates of burned biomass are generated from EO-derived metrics of burned area (BA), active fire counts and/or fire radiative power (FRP). These burned biomass estimates are multiplied by biome-specific emission factors (EFs) to relate each kilogram of burned dry matter to the amount of a trace gas or aerosol released into the atmosphere. EFs are mostly derived from small scale laboratory or ground-based field measurements (Andreae and Merlet, 2001; Akagi et al., 2011; Andreae, 2019), and more rarely through airborne sampling of larger plumes (Abel et al., 2003; Lavrov et al., 2006; Quennehen et al., 2012). ‘Bottom up’ emissions inventories include GFED (Van Der Werf et al., 2006, 2010, 2017), GFAS (Kaiser et al., 2012), FLAMBE (Reid et al., 2009) and FINN (Wiedinmyer et al., 2011). Biases and uncertainties present in these landscape fire inventories stem primarily from:

i) Limitations of the original satellite observations and the fire detection and characterisation algorithms applied to them to generate the EO-derived fire metrics. Compromises are generally made between spatial and temporal resolution, and algorithm errors of omission and commission impact the precision and accuracy of the EO-derived fire measures (Boschetti et al., 2004; Freeborn et al., 2009; Randerson et al., 2012).

ii) Assumptions associated with estimating the fuel consumption per unit area ($kg.m^{-2}$) or any alternative scalar required to turn the EO-derived metric into an estimate of burned dry matter (Kasischke and Penner, 2004; Reid et al., 2009; Wooster et al., 2011; Kaiser et al., 2012)

iii) Limitations in the EFs used to convert between burned dry matter and the final emissions of aerosols and trace gases (Van Leeuwen and Van Der Werf, 2011).

Addressing (i) above, advancements continue to be made to the EO-derived fire metrics extracted from data collected by polar-orbiting sensors such as MODIS and VIIRS (e.g. Schroeder et al., 2014; Giglio et al., 2016; Zhang et al., 2017), and by geostationary sensors such as Meteosat SEVIRI and Himawari-8 AHI (Wooster et al., 2015) and in the case of (iii), more detailed EFs are regularly being proposed (e.g. Akagi et al., 2011; Huijnen et al., 2016; Andreae, 2019). However, arguably less research has focused on (ii), namely, how to improve estimates of burned dry matter derived from burned area, active fire (AF) detection or FRP data products. Despite this being considered to be the step introducing probably the greatest uncertainties in ‘bottom-up’ approaches (Reid et al., 2009; Ichoku and Ellison, 2014; Mota and Wooster, 2018). Partly for this reason, fully ‘top-down’ methodologies such as those of Ichoku and Ellison (2014) and Mota and Wooster (2018) have taken to deriving landscape fire emissions estimates directly from EO-derived FRP measures, thereby bypassing the fuel consumption estimation step altogether and reducing the number of assumptions required during the fire emissions calculation. In these approaches, a biome-dependent scalar (a smoke emission coefficient; C_e in $g.MJ^{-1}$) captures the relationship between the FRP of fires and their associated total particulate matter (TPM) emissions. These coefficients are derived from a series of matchup fires where FRP data and satellite aerosol optical depth (AOD) observations are available in the biome of interest. Once this scalar is determined, the need to calculate fuel consumption is removed when deriving further smoke emissions estimates from the FRP data of observed fires. Whilst these 'top-down' approaches successfully bypass the fuel consumption step, in both the Fire Energetics and Emissions Research (FEER; Ichoku and Ellison, 2014) and Fire Radiative Energy Emissions (FREM; Mota and Wooster, 2018) approach, the coarse 10 km spatial resolution of the MODIS AOD product used to derive in-plume TPM, and performance issues related to this AOD product in thick-smoke affected environments, can introduce significant problems when deriving the smoke emission coefficients. To address this problem, we here present a series of improvements to the FREMv1 methodology of Mota and Wooster (2018) and use this (FREMv2) method to produce a new Meteosat SEVIRI FRE-based fire emissions inventory for the whole of Africa. A series of methodological evolutions are presented, key of which is the exploitation of a far higher spatial resolution (1 km) MODIS AOD product (Lyapustin et al., 2018) that offers improved performance in heavily smoke impacted environments.

2. FIRE EMISSION INVENTORY METHODOLOGIES

2.1 ‘Bottom-up’ Total Fuel Consumption (F_c) Based Methodologies

Most widely used ‘bottom-up’ fire emission inventories currently take their emission factors (EFs in $g.kg^{-1}$) from those collated by Andreae and Merlet (2001), although recent updates are reported in Andreae (2019). Therefore, inter-inventory variations in both total fire emissions magnitude and spatio-temporal distribution originate primarily not from the EFs used, but in the estimation of total fuel consumption (F_c), often called dry matter consumed (DMC). The uncertainty in DMC estimates primary stems from limitations (i) and (ii) introduced in Section 1. These are performance issues in the EO data products (typically BA or FRP) used to characterise the biomass burning, and the assumptions made when estimating DMC from these (e.g. Wooster et al., 2011; Knorr et al., 2012; Larkin et al., 2014).

In the Burnt Area (BA) approach to estimating total fuel consumption (Seiler and Crutzen, 1980), DMC is estimated via multiplication of BA [m^2], fuel load [FL; $kg.m^{-2}$] and combustion completeness [CC; unitless]. BA measures are typically taken from the 500 m spatial resolution MODIS MCD64A1 product (Giglio et al., 2018), with the parameters of fuel load and combustion completeness either taken from literature values (e.g. Reid et al., 2005) or the outputs from vegetation growth models (GFED; van der Werf et al., 2006). In addition to uncertainties in the fuel load and combustion completeness parameters (Reid et al., 2009; Vermote et al., 2009; Van Leeuwen and Van Der Werf, 2011), many small fires appear to remain unmapped in MCD64A1 (Tsela et al., 2014; Hawbaker et al., 2017; Roteta et al., 2019). A widely used BA-based fire emissions inventory is the Global Fire Emissions Database (GFED; Van Der Werf et al., 2006), providing emissions at 0.25˚ grid cell resolution. The latest version (GFEDv4.1s; Van Der Werf et al., 2017) uses MODIS active fire (AF) detections to ‘boost’ the BA values in an attempt to compensate for small fires remaining undetected by MCD64A1 (Randerson et al., 2012). Whilst

MCD64A1 BA totals clearly need to be raised in some way, this ‘boosting’ process can introduce biases in BA in regions that are, for example, dominated by interspersed agricultural and urban areas (Zhang et al., 2018).

In the FRP-based approach to estimating dry matter consumed, FRP observations are temporally integrated to estimate Fire Radiative Energy (FRE), which in small-scale fires has been shown to directly relate to DMC (Wooster et al., 2005; Freeborn et al., 2008; Ichoku et al., 2008). A conversion factor ($g.MJ^{-1}$), typically derived from these small-scale fires (e.g. that of Wooster et al. (2005)) is then used to convert satellite-based FRE measures into DMC estimates (Roberts et al., 2005, 2011). This removes the need for assumptions about the poorly constrained parameters of fuel load and combustion completeness that are required by methods using BA data – but relies on the fact that the conversion factor derived from small scale fire experiments remains valid at the scale of landscape fires observed from satellites. This may be an unrealistic assumption, particularly in certain landscapes (Mota and Wooster, 2018). For example, tree canopy cover may intercept a significant percentage of the fire-emitted FRP in more forested regions, leading to lower spaceborne FRP measurements (Freeborn et al., 2009; Mota and Wooster, 2018; Roberts et al., 2018a). A positive benefit of satellite AF products are that they are sensitive to small fires covering as little as 10^{-4} of the pixel area (Roberts et al., 2005), hence the contribution of relatively small fires is typically included in FRP-based fire products, provided they are burning at the time of the satellite observation. This compares to most satellite BA products, where generally > 20% of the pixel area must be fire affected for a burn scar to be reliably detectable (Giglio et al., 2006, 2009), but with the advantage that the burned area remains detectable and measurable for some time after the fire has ceased.

For providing near-real time fire emissions estimates, BA-based approaches are, in any case, usually inappropriate since the required burned area, FL and CC datasets are typically only available with significant time-lag. This is one further reason why FRP-based approaches are becoming more common, since satellite FRP data of a fire are typically available within minutes to hours depending on the observation system. A widely used FRP-based fire emissions inventory is the Global Fire Assimilation System (GFAS; Kaiser et al., 2012). GFAS provides daily data at 0.1˚ globally as part of the Copernicus Atmospheric Monitoring Service (CAMS: https://atmosphere.copernicus.eu/). In GFAS, weighted mean FRP values from MODIS MOD/MYD14 products (Justice et al., 2002; Giglio et al., 2003) are used to derive daily FRE estimates (assuming either a flat FRP emissions profile or a standard fire diurnal cycle), which are then multiplied by biome-specific conversion factors (in $kg.MJ^{-1}$) relating FRE to DMC (Kaiser et al., 2012). These GFAS-specific conversion factors are based on prior comparisons between the MODIS-based GFASv1.0 FRE estimates and the BA-derived DMC totals of GFEDv3.1 (Van Der Werf et al., 2006, 2010), which themselves come from an adaption of the original Seiler and Crutzen (1980) approach (Heil et al., 2010). In this way, GFAS fire emissions estimates are not only influenced by GFEDs biases and uncertainties in fuel load, combustion completeness and unmapped small burned areas (Reid et al., 2009; Vermote et al., 2009), but are also directly dependent on the GFED DMC estimates themselves (Kaiser et al., 2012). The operational GFAS also uses only polar-orbiting satellite FRP data, currently that from MODIS, somewhat limiting its temporal resolution and the accuracy of any FRP-to-FRE conversion.

2.2 FRP Datasets for Emissions Estimation

The FRP measures derived from the polar-orbiting (MODIS) sensors used within GFAS and elsewhere fail to capture the full diurnal cycle of a fire, and must typically be interpolated between observations or used to scale an assumed diurnal cycle in order to estimate FRE (Freeborn et al., 2009; Vermote et al., 2009). It is however possible to use the very high temporal resolution FRP data available from geostationary satellites to provide almost continuous FRP observations, and these can then be accurately and easily integrated to calculate FRE without any assumptions on the shape of the fire diurnal cycle (e.g. Wooster et al., 2015). The main limitation of geostationary FRP datasets is that the minimum FRP detection limit, below which actively burning fires remain undetected, is higher than for most polar-orbiting sensors due to the larger geostationary pixel areas (Roberts et al., 2005, 2015). However, the detectable AFs in geostationary products still remain significantly smaller in terms of pixel area coverage (e.g. down to perhaps 0.01% of the pixel) than the minimum burned area detectable in the MODIS BA products. Another disadvantage of geostationary active fire data is that geostationary pixel areas grow markedly at locations very far from nadir (> 40° view zenith angle), so high latitude regions are generally less well suited to geostationary FRP analysis. A recent evaluation of geostationary active fire data was carried out by Hall et al. (2019) who compared AF detections within the Meteosat SEVIRI FRP-PIXEL product used herein (see Section 4) to those identified in 30 m spatial resolution Landsat-8 Operational Land Imager (OLI) data (Hall et al., 2019). Results for the AF error of commission showed this to be 8% for the SEVIRI product compared to OLI, a false alarm rate very similar to that of the widely used MODIS AF products (Giglio et al., 2013; Schroeder et al., 2014). AF errors of omission for the SEVIRI product were however 98% compared to OLI, but the 30 m OLI pixel size enables fires covering just a few square meters to be detected, compared to the roughly one thousand square meters required for detection with SEVIRI assuming an AF detection limit of 0.01% of the pixel area. Thus, a large number of very small fires can be detected by OLI that remain essentially impossible to detect by SEVIRI. Comparison between the SEVIRI FRP-PIXEL AF product and 1 km MODIS AF data have been commonly performed (Roberts and Wooster, 2008; Roberts et al., 2015) and the SEVIRI AF error of omission rate in such comparisons is far lower than when OLI is used as the reference dataset (Roberts et al., 2015). Indeed, Wooster et al. (2015) indicate that over the lifetimes of most African fires, active fires detected by MODIS become detectable by SEVIRI at some point in their diurnal cycle. The Hall et al. (2019) study also highlights that, though at any given time the higher spatial resolution polar orbiter-based FRP products are likely to detect more fires than geostationary based products due to their ability to detect lower FRP fires, the increased temporal resolution provided from geostationary orbit typically results in far more AF detections overall, during a 24 hour period.

2.3 Top-down FRP-based Methodologies

The FREMv1 approach to fire emissions estimation (Mota and Wooster, 2018) is an FRP-based calculation, classed as a 'top-down' method since it only uses satellite observations (specifically geostationary FRP and polar orbiting-derived Aerosol Optical Depth [AOD] data). The method avoids problems inherent in the intermediate DMC estimation step of the 'bottom-up' approaches (Section 2.1), though fuel consumption in terms of total DMC or its combustion rate can still be calculated as a final output (see Mota and Wooster, 2018). Whilst the GFAS system (Kaiser et al., 2012) is also based on FRP data, it is not fully top down as it relies on conversion coefficients between FRP and DMC that come from BA-based approaches which themselves rely on model-based fuel load and combustion completeness variables (Van Der Werf et al., 2006, 2010). The FREM approach is somewhat similar to the fire emissions estimation approach introduced by Ichoku and Kaufman (2005) in that it directly links FRP data to emissions of total particulate matter, albeit FREM uses geostationary rather than polar-orbiting FRP data for the reasons discussed in Section 2.2. Ichoku and Kaufman (2005) and follow-up work by Ichoku and Ellison (2014) took both their FRP and AOD data from the polar-orbiting MODIS sensor, and used these datasets to deliver the Fire Energetics and Emissions Research (FEER) smoke emission product. In the FEER and FREM approaches to fire emissions estimation, as well as in the other top-down methods of Lu et al. (2019) and Darmenov and da Silva (2015), the intermediate step of estimating

DMC (kg) or dry matter combustion rate (kg.s^{-1}) is bypassed by deriving a 'smoke emission coefficient' [C_e] describing the relationship between the thermal energy a fire radiates (i.e. the FRE in MJ) and the mass of total particulate matter (TPM in kg or g) it emits, or between the rates of these two (i.e. the FRP in MW and the TPM emission rate in g.s^{-1}). C_e has units of g.MJ^{-1} or g.s^{-1}.MW^{-1} respectively in each case, and is itself typically derived from a set of matchup fires for which good observations of both variables exist. To derive C_e, each matchup fire has its TPM estimated using satellite observations of AOD, or from modelled AOD in the case of Darmenov and da Silva (2015). Once C_e is determined using these matchup fires, it can be applied to the FRE or FRP data of all fires to estimate their TPM emissions or emissions rate as well. FEER and Lu et al. (2019) use MODIS FRP data as opposed to FREM's geostationary FRP data, and therefore can be affected by MODIS's over-or-under estimation of FRE due to its limited temporal resolution as discussed in Section 2.2 (Kaiser et al., 2012; Andela et al., 2015). The "bow tie effect" caused by the sensor's design and scanning geometry can also affect the estimation of FRE from FRP measures (Freeborn et al., 2011; Wiedinmyer et al., 2011). Proposed methods to address the estimation of FRE from MODIS FRP assume that the MODIS Aqua early-afternoon overpass roughly coincides with, and captures, the peak of daily fire activity, and can therefore be used to parameterise a diurnal cycle that provides interpolation-based higher temporal frequency estimates of FRP (Ellicott et al., 2009; Vermote et al., 2009). However, due to the considerable spatial variability seen in both fire diurnal cycles (Giglio, 2007) and the local MODIS Aqua overpass time, the time difference between the peak of fire activity and the MODIS overpass varies both geographically and daily, as does the fraction of total daily fire pixel counts occurring at the MODIS overpass (Mota and Wooster, 2018). In cases where the latter is particularly low, polar-orbiting based calculations of daily FRE are susceptible to a low bias, but when the MODIS overpass coincides closely with peak fire activity this is less pronounced. Such spatial variations can lead to artificial differences in the derived daily FRE (Mota and Wooster, 2018), and this is one justification for the use of geostationary-derived FRP data in the FREM approach. Furthermore, in the FEER approach of Ichoku and Ellison (2014) and in the Lu et al. (2019) methodology, the AOD and FRP observations of the matchup fires used to derive the C_e coefficients are based on MODIS observations of the plume and actively burning fire that are acquired at exactly the same time. This inherently means that the TPM contained within the plume (which has been emitted since the fire commenced up to the time of the MODIS overpass) is being related to the FRP the fire is releasing at the moment of the overpass. This is a potential disadvantage, because earlier on in the fire lifetime – during which most of the TPM was actually released - the fire might have had a quite different FRP to that at the time of the MODIS overpass. The FREM approach avoids this problem by using geostationary FRP observations and integrating these over time to calculate the FRE released by the fire from the time it started until the time of the MODIS overpass providing the AOD-based TPM estimate. Furthermore, by subsequently applying the C_e coefficients to all the geostationary FRP data, not just the matchup fires, very high temporal resolution fire emissions estimates can be generated, which can be important for (i) capturing sub-daily variability in fire and smoke emissions (Roberts et al., 2015), and (ii) delivering the most accurate modelling of atmospheric pollutant dispersion and peak air pollutant concentrations in large fire events (Baldassarre et al., 2015).

2.4 Further limitations in current top-down methodologies

In all previous top-down methodologies, biome dependant (e.g. FREMv1) and/or geographically dependant (e.g. FEER) smoke emission coefficients have been derived using satellite-based FRP observations and the 10 km AOD (MOD/MYD04) MODIS Level 2 product from Terra (~10:30 overpass) and Aqua (~ 13:30 overpass) (Ichoku and Kaufman, 2005; Ichoku and Ellison, 2014;

Mota and Wooster, 2018; Lu et al., 2019). The outputs of two different AOD retrieval algorithms are available in this MODIS product;

i) Dark Target (DT): designed to work over dense vegetation.

ii) Deep Blue (DB): developed for desert surfaces but updated to apply to most cloud free land.

Output from Dark Target was used by Ichoku and Kaufman (2005) and Ichoku and Ellison (2014), whereas Mota and Wooster (2018) and Lu et al. (2019) use Deep Blue (introduced in Collection 6) since it showed better agreement with AREONET AOD observations across southern Africa (Sayer et al., 2014).

The MODIS 10 km AOD (MxD04) product and its updates (Tanre et al., 1997; Hsu et al., 2004, 2006, 2013; Remer et al., 2005; Levy et al., 2013) has been produced for more than 15 years, are widely used within the air quality community (Remer et al., 2013), and have been extensively characterised and validated (Holben et al., 2001; Chu et al., 2002; Ichoku et al., 2002, 2003; Sayer et al., 2013; Livingston et al., 2014; Xiao et al., 2016; Jethva et al., 2019). However, their use in top-down fire emissions inventories introduce some key uncertainties and limitations, including those associated with its relatively low 10 km spatial resolution (Lyapustin et al., 2011; Raffuse et al., 2013; Remer et al., 2013; He et al., 2017), the cloud mask implemented in both the DT and DB versions (Levy et al., 2013; Raffuse et al., 2013; Remer et al., 2013; Livingston et al., 2014), and MODIS view-angle effects (Sayer et al., 2015). The more recent 3 km MODIS AOD product which applies the Dark Target retrieval algorithm (Remer et al., 2013) also suffers from distortions at wide swath angles and erroneous cloud masking over thick smoke.

AOD retrievals in the MxD04 product are produced at 10 km to improve the signal-to-noise ratio of the input reflectance data (Tanre et al., 1997). In the Deep Blue retrieval, henceforth referred to as MxD04_DB, the original 1 km pixels are arranged into 10 $\times$ 10 pixel blocks and screened to remove those affected by cloud. The remaining pixels in each 10 km block are then used to deliver the AOD retrieval (Hsu et al., 2013), and the number of 1 km pixels used accompany the final 10 km AOD estimates contained within the product. When targeting smoke plumes, our investigations and those of other studies (e.g. Levy et al., 2013; Livingston et al., 2014) show that the conservative cloud mask used by both the DT and DB algorithms result in cases of (i) the 10 km AOD estimates at the locations of the thickest smoke being completely masked out, and (ii) the 10 km AOD estimates in areas of thick smoke being retrieved from only a fraction of the 1 km pixels present within the 10 km $\times$ 10 km box. Figure 1 demonstrates an example of a smoke plume where some MxD04_DB pixels use as little as 40% of the original one hundred MODIS 1 km pixels to retrieve a single 10 km AOD value, though at wide swath other distortions occur and pixels are in fact not 10 km^2. A comparison with the 500 m MODIS true colour image for the same area (Fig. 1c) demonstrates how the low spatial resolution of the MxD04_BD product introduces further uncertainty into the determination of the plume boundary, particularly when compared with the alternative 1 km MAIAC AOD product (Fig. 1d) discussed in Section 3.

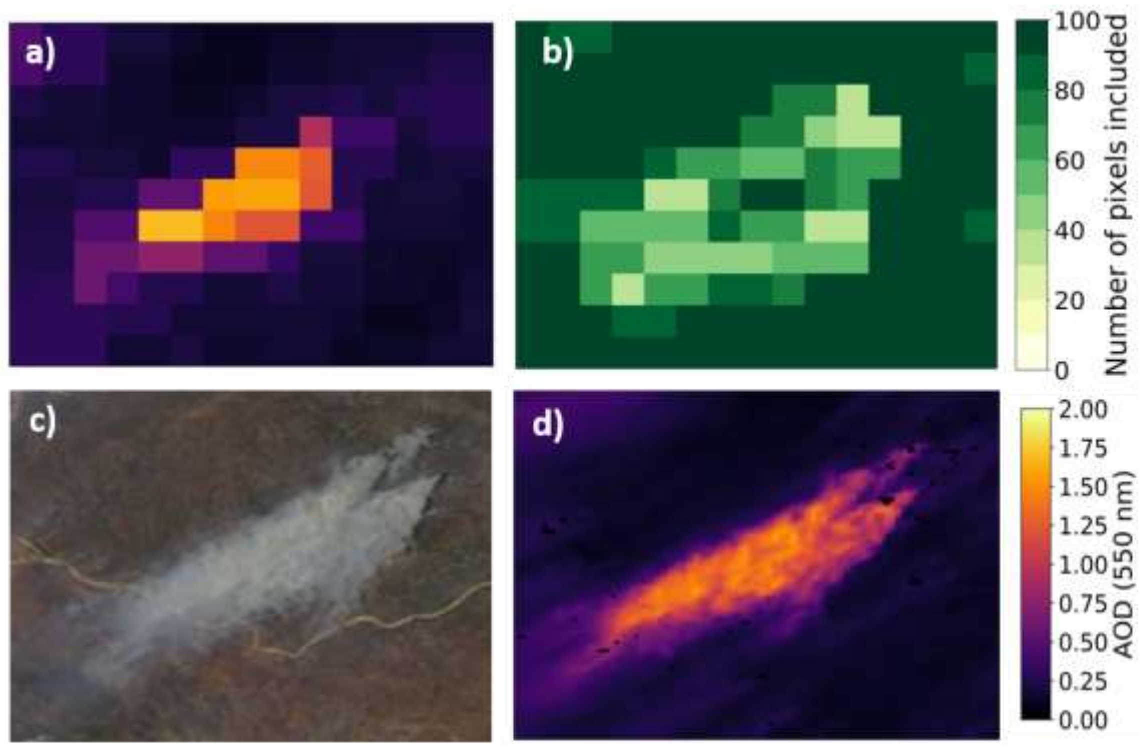

(1.5 columns) **Figure 1**. Example plume from a fire burning north of the Save River (Mozambique), imaged on the morning of 8th October 2015 at 11:15 UTC via the Aqua satellites MODIS sensor (at a VZA 40.6°). (a) 10 km MxD04_DB AOD product; (b) MxD04_DB field showing the number of 1 km reflectance pixels (out of 100) used to retrieve each 10 km AOD pixel value; (c) 500 m MODIS Corrected Reflectance (True Colour) image; and (d) 1 km MCD19 MAIAC AOD product derived from the same MODIS imagery shown in (c). The colour scale shown in (d) is also relevant for (a). The plume is far more easily distinguished in the 1 km than the 10 km AOD product and better matched to the smoke spatial distribution shown in the MODIS true colour image of (c). Unlike the 1 km AOD product of (d), the 10 km MxD04_BD AOD data of (a) rather poorly defines the plume bounds and some pixels in this product are heavily impacted by the cloud mask which removes AOD pixels over the thickest smoke (b). Some erroneous masking does occur in the 1 km product of (d), shown as the black pixels, but this is minimal and addressed via the interpolation described in Section 4.3.

The extreme masking of smoke affected 1 km pixels as cloud in the MxD04_DB algorithm, as demonstrated in Figure 1, introduces clear uncertainty and probably bias into any estimates of total particulate matter (TPM) derived from the 10 km MxD04 AOD observations. Since the excluded pixels are mainly located over the thickest smoke, their exclusion is likely to significantly affect the final retrieved 10 km AOD, and therefore the TPM measure. Additionally, the complete masking of 10 km pixels in some cases limits the number of plumes that can be identified and used in deriving the FREM smoke emission coefficients. Both Mota and Wooster (2018) and Lu et al. (2019) take measures to try and minimise the effect of completely masked MxD04_BD pixels. Mota and Wooster (2018) keep MxD04_BD pixels with quality mark ≥ 2, resulting in MxD04_BD pixels using as little as 40% of the native 1 km pixels being retained (e.g. in Fig. 1b), and they also excluded plumes comprising any completely masked 10 km pixels. Lu et al. (2019) use a nearest neighbour method to fill gaps in the data over plumes, which are caused by erroneously ‘cloud masked’ AOD pixels.

Another source of uncertainty introduced when using either the MODIS DT or DB MxD04 product comes from the MODIS ‘bowtie’ effect that results from the MODIS design and scan geometry, along with Earth’s curvature (Wolfe et al., 1998). Above view zenith angles (VZA) of $\sim 20^{\circ}$, two key distortions occur with respect to MxD04_BD - (i) growth of the MODIS 10 km AOD ‘pixel’ area from about 10 × 10 km at nadir to around 20 × 40 km at the scan edge, and (ii) the overlap of successive scans towards the scan edge meaning features are duplicated in adjacent pixels (Wolfe et al., 1998). Both result in an AOD data product rather dependent on the location of the AOD pixels within the MODIS swath, and there are indications that this may influence the statistics of the AOD retrievals towards the scan edges (Sayer et al., 2015), potentially introducing bias into top-down methodologies using the MxD04 AOD products without excluding high-VZA observations during derivation of their C_e values.

A further significant limitation of the MxD04 AOD products relate to their fundamentally low 10 km (at nadir) spatial resolution (see Figure 1), which is unable to resolve smoke plumes from many smaller fires, or from fires not sufficiently isolated from other aerosol sources (primarily other nearby fires). In both cases, differences between the in-plume AOD and the background AOD (i.e. the AOD anomaly) may not be significant enough to define the AOD pixels that represent the plume. This both places a limit on the minimum fire size used to derive C_e or C_{biome} values and makes the sampling of fires over certain areas during periods of peak fire activity difficult, as their plumes often merge together (Mota and Wooster, 2018).

Separate from the MxD04 AOD product issues, differences in the method chosen to calculate the value of an AOD background exist between top-down methodologies. In all top-down inventories discussed herein, the equations proposed by Ichoku and Kaufman (2005) are used to convert AOD to the emitted TPM of an individual fire. The fire emitted AOD for a given smoke plume is defined as the summed total AOD of the smoke plume above the AOD background (for full details see Ichoku and Kaufman, 2005). It is clear then, that the choice of AOD background value used in these calculations impacts the final TPM estimate, and therefore the C_e or C_{biome} values derived from matchups between these values and the corresponding fire FRE. Ichoku and Kaufman (2005) and Ichoku and Ellison (2014) select background AOD values based on pixels immediately up-wind of the smoke plume, whereas Mota and Wooster (2018) take background AOD values to be the 20th percentile AOD of all values within a set distance or area (e.g. 500 km^2) surrounding a fire. The background AOD values estimated from this large-scale averaging may not be fully representative of the true background into which a plume is being emitted, and so may also negatively impact the derived C_{biome} values in FREMv1.

The above problematic characteristics of the MxD04 products, and the FREMv1 and FEER methodologies, contribute to uncertainty and possibly bias in the smoke emission coefficients derived, and thus to the resultant smoke emissions estimates. We here focus on developments to FREMv1 to try to mitigate these impacts.

3. DEVELOPMENTS TO THE FREM APPROACH

The methodology proposed here builds on the original FREMv1 approach of Mota and Wooster (2018) to address the limitations described in Section 2.3. A key advance is use of an alternative MODIS AOD product that offers substantial advantages over the MxD04 products when used in smoke-affected areas. This alternative AOD product is based on the Multiangle Implementation of Atmospheric Correction (MAIAC) algorithm, developed to retrieve surface bidirectional reflectance factor (SBRF), internal cloud mask and AOD over land (Lyapustin et al., 2011). The MAIAC AOD product provides combined Aqua and Terra AOD retrievals at a 1 km resolution over both dark and bright surfaces, and has been shown to improve the resolvability of atmospheric smoke and dust features compared to the 10 km MxD04 product (Emili et al., 2011; Lyapustin et al., 2011, 2012; Jethva et al., 2019; Mhawish et al., 2019). At AERONET station locations, both Emili et al. (2011) and Jethva et al. (2019) show that the MAIAC product provides more than double the number of AOD retrievals compared to MxD04_DB, due to its higher spatial resolution and improved cloud mask. In fact, the MAIAC algorithm explicitly includes a ‘smoke test’ to discriminate biomass burning smoke from clouds (Lyapustin et al., 2012). Other evaluations have compared the MAIAC product to the Visible and Infrared Imaging Radiometer Suite (VIIRS) 750 m spatial resolution AOD product, to AERONET measurements, and to surface measurements of particulate matter (Hu et al., 2014; Arvani et al., 2016; Martins et al., 2017; Superczynski et al., 2017). They have shown its improved coverage compared to the standard VIIRS AOD product and its good agreement with ground-based AOD and particulate matter measures.

In addition to its higher spatial resolution and improved cloud mask, some key features of the MAIAC product address issues related to the dependence of AOD retrievals on VZA in the MxD04 product. These include the gridding of L1B MODIS bands to 1 km resolution prior to AOD retrieval using an area-weighted method (Wolfe et al., 1998), and the calculation of surface BRF using a dynamic spectral regression coefficient (SRC) (Lyapustin et al., 2011). The former results in an improved representation of any given 1 km grid cell by appropriately weighing the contribution of observations falling within that cell, and this is especially important at the swath edge where the MODIS pixel area is up to eight times larger than at nadir. The dynamic SRCs, are calculated from a time series analysis of previous AOD retrievals for each 1 km pixel. Therefore, when VZA are well sampled in the preceding retrieval times series (multiple cloud free observations per pixel), SRC values represent well the angular component of surface BRF (full details can be found in Lyapustin et al. (2011)). The final MAIAC AOD product is reported on a 1 km grid in the MODIS sinusoidal projection (Lyapustin et al., 2018) and Mahawish et al. (2019) show VZA-dependant bias to be the lowest in MAIAC AOD retrievals compared to the output of the MxD04 DT and DB algorithms. Figure 2 shows fire emitted TPM estimates for a series (n=635) of African smoke plumes, as derived from the MxD04_DB AOD product and the MAIAC AOD product, all calculated via multiplication of the plume-integrated AOD anomaly (accounting for pixel area) by the smoke mass extinction coefficient (following Ichoku and Kaufman (2005)). Whilst the MAIAC-derived TPM estimates appear consistent across all VZA's, those from MxD04_BD increase significantly at VZA > 40˚. Inclusion of plumes observed at high VZA values in the MxD04_DB product used by Mota and Wooster (2018) could lead to artificially high in-plume TPM estimates, and therefore a high bias in the derived C_e or C_{biome} values in FREMv1. When a comparison is made between MxD04_BD and MAIAC estimated TPM from plumes with VZA < 20° (Fig 2b.), MAIAC-based TPM estimates are typically higher (on average by ~ 26%) than those of MxD04_BD. This likely results from the less conservative MAIAC cloud mask and the increased number of valid AOD retrievals available over the thickest smoke when compared to MxD04_BD.

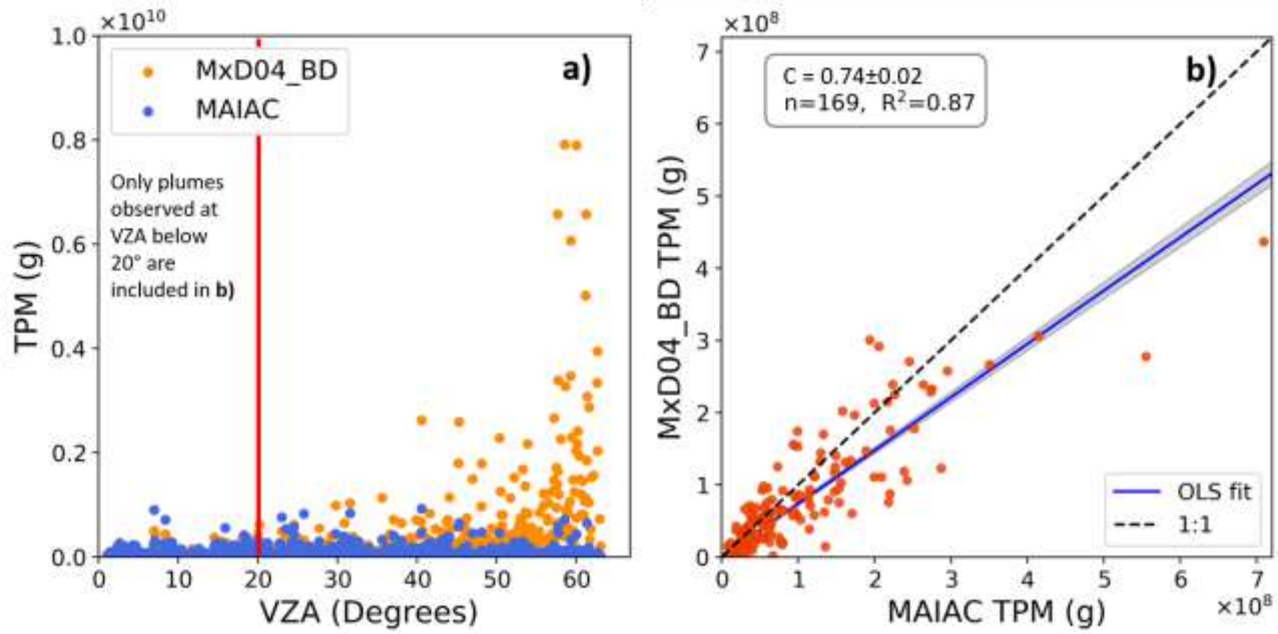

(1.5 columns) **Figure 2.** (a) Estimated fire emitted Total Particulate Matter (TPM) in 635 individual smoke plumes, as derived from the 10 km MxD04_DB AOD product (*orange*) and the 1 km MAIAC AOD product (*blue*), shown as a function of sensor view zenith angle (VZA). (b) Direct comparison of the matching MxD04_DB and MAIAC-derived TPM values for each plume, restricted to plumes observed at VZA ≤ 20˚. TPM is calculated from AOD using the equations presented in Ichoku and Kaufman (2005) as described in Section 4.4.

Another update performed in FREMv2 compared to FREMv1 is an improved method for calculating the background AOD value of smoke plumes. FREMv2 applies a localised value for background AOD, as opposed to the large-area-average value applied in FREMv1. The minimum AOD pixel within a buffered area of the smoke plume, in most cases, up-wind of the targeted plume is used as the background AOD value. This approach is similar to that adopted by Ichoku and Kaufman (2005) and Ichoku and Ellison (2014), and justified by the argument that (i) background AODs derived from large scale averaging could be biased by reflectance anomalies or aerosol changes far from the plume, for example dust in the averaging area, and (ii) a large-area-averaged background will also be insensitive to the immediate local AOD background of the plume (e.g. during periods of high fire activity when atmospheric particulate matter concentrations are likely to locally be high already).

Other adjustments in FREMv2 include the consideration of relative humidity in the estimation of fire generated TPM, expansion to the entirety of continental Africa, and the inclusion of more up-to-date land cover and % tree cover information to delineate more precisely the fire-relevant biomes, details of which are included in Section 4.

4. SMOKE EMISSION COEFFICENTS DERIVATION

4.1 Geographic Area and Biome Classification

For derivation of the biome-dependent FREMv2 smoke emission coefficients (C_{biome}) and final emissions estimates, we expanded the Southern Hemisphere Africa (SHAf) region of Mota and Wooster (2018) to include Northern Hemisphere Africa (NHAf). In SHAf the dry season is July to September, and in NHAf November to April, periods which also represent the primary fire seasons in these regions. The dense tropical forests close to the equator (e.g. in northern D.R.C and Gabon) are wetter and less susceptible to large-scale fires compared to those dominated by deciduous and herbaceous vegetation further north and south. These woody savannah and shrubland/grassland areas are those that host most of Africa's biomass burning. In addition to expanding FREMv2 to continental Africa, we also deployed an updated landcover map to provide more detailed biome classification. The 2015 European Space Agency (ESA) Climate Change Initiative (CCI) Landcover map (Validated by ESA (2017)) is derived from 300 m spatial resolution PROBA-V observations and comprises 36 landcover type, which we aggregate into five distinct biome classes. Following Mota and Wooster (2018), grassland and woodland savanna are classified as separate biomes as suggested by Korontzi et al. (2004) for fire-related GHG emission reporting. Full details of the CCI land cover class assignment for the FREMv2 biomes can be found in Appendix A. Five biomes were defined by the main vegetation types of *closed canopy forest*, *woodland savanna/open forest*, *grassland*, *shrubland* and *managed lands*. Since the biome classes of FREMv1 were based on the GLOBCOVER 2009 landcover map (http://due.esrin.esa.int/), which differs from the 2015 CCI landcover map in some respects, the spatial distribution of our biome classes also differ, for example in the Kalahari region of southern Africa. To provide further biome discrimination, FREMv2 also includes use of percentage tree cover (above 5 m height), taken from the 30 m Landsat Vegetation Continuous Fields (VCF) product of 2015 (https://landsat.gsfc.nasa.gov/) (Fig. 2a). Since woodland savanna is by far the largest contributing biome to FRE release over Africa (Appendix B), correct assessment of its smoke emissions is critical to overall accuracy. Areas of woodland savanna having higher tree cover, though still dominated by surface fires (van Leeuwen et al., 2014), have the potential to produce smoke plumes more influenced by surface litter and woody debris (Heil et al., 2010). They may also be more affected by canopy interception of surface-emitted FRP (Freeborn et al., 2009; Roberts et al., 2018a). Hence, to improve the precision of C_{biome} values for woodland savanna fires, we separated this class into *low-woodland savanna* and *high-woodland savanna* using a 20% VCF tree cover threshold.

The FREMv2 biome map was re-projected and aggregated to the Meteosat SEVIRI full disk projection, such that each SEVIRI pixel was assigned a sub-pixel fraction of each biome, with the overall pixel class assigned to the majority fraction (Fig. 2b). Locations of the closed canopy forest and low- and high-woodland savanna biomes (the main classes having vegetation above 5 m height) broadly match the % tree cover spatial distribution of VCF product (Fig 2a), and also agree well with tree cover maps derived previously from MODIS data (e.g. Hansen et al., 2002; Sexton et al., 2013; Kobayashi et al., 2016).

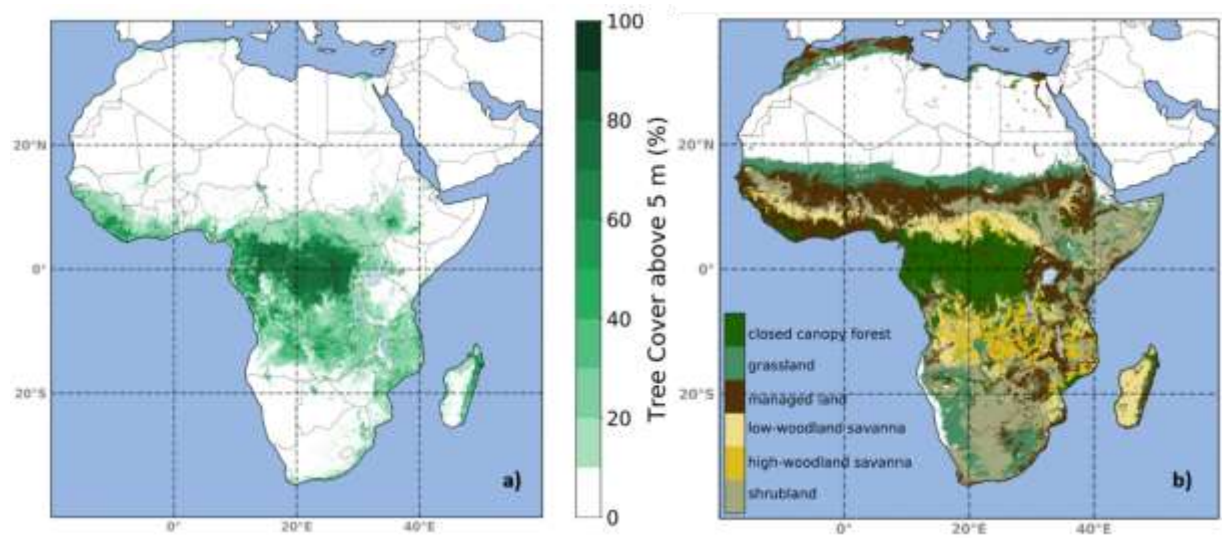

(2 columns) **Figure 3.** (a) Mapped percentage tree cover above 5 metres, as determined from the 30 m spatial resolution Landsat Vegetation Continuous fields (VCF) product for 2015. (b) FREMv2 biome map for Africa derived from the 2015 ESA CCI Landcover map (itself derived from 300 m PROBA-V imagery) and the Landsat VCF product. Biomes were aggregated from the 36 land cover types defined in the original CCI map, with the two woodland savanna biomes separated using (a) (see Appendix A).

4.2 FRP and AOD 2015 Datasets and Fire Matchups

The geostationary Meteosat SEVIRI FRP-PIXEL product of Wooster et al. (2015) was a primary input for derivation of the C_{biome} values. The full spatio-temporal resolution (15 min, 3 km at nadir) FRP-PIXEL product covering the NHAf and SHAf fire season of 2015 was acquired from the EUMETSAT Land Surface Analysis Satellite Applications Facility (LSA SAF: http://landsaf.meteo.pt). The AOD product used was the Terra and Aqua combined MODIS MAIAC 550 nm 1 km product (Collection 6 MCD19A2; Lyapustin et al., 2018), described in Section 3.

Fire activity from the FRP-PIXEL product was assigned to MAIAC AOD measurements of smoke plumes in what we refer to here as 'fire matchup selection'. First, a blob detection (Difference of Gaussian; Lindeberg , 1998) procedure commonly used in computer vision was applied to each MAIAC AOD image to identify regions of interest (ROIs) containing potential smoke plumes. These ROIs were filtered to keep only those having active fires (spatially contiguous FRP pixels observed between 00:00 local time and the MODIS overpass used to produce the MAIAC product) in close spatial proximity. To ensure complete sampling of all fire activity contributing to a given smoke plume, the FRP-PIXEL Quality Product detailed in Wooster et al. (2015) was used to filter out fires that were cloud-obscured leading up to the MODIS overpass time. In cases when both Aqua and Terra MAIAC AOD data were available, the Aqua data acquired closer in-time to the peak of the fire diurnal cycle were preferentially used. This subset of candidate fire matchups was subject to a final manual check to remove any erroneously identified or poorly defined plumes.

Each remaining ROI containing a smoke plume had the AOD boundary of the plume defined via histogram thresholding of AOD pixel values (Fig. 4a and 4b). The convex hull of the plume feature was used to define the plume edges and all FRP pixels measured within this bound, between 00:00 hrs and the MODIS overpass time relevant to the AOD product, were categorised as being from the fire which contributed smoke to the plume (Fig. 4c). Though in most of cases FRP pixels were not observed until 08:00 local time. The 1 km resolution of the MAIAC data meant analysis of plume RBG imagery was not needed to help define plume features, unlike with the 10 km MxD04_DB data used in FREMv1 (Mota and Wooster, 2018).

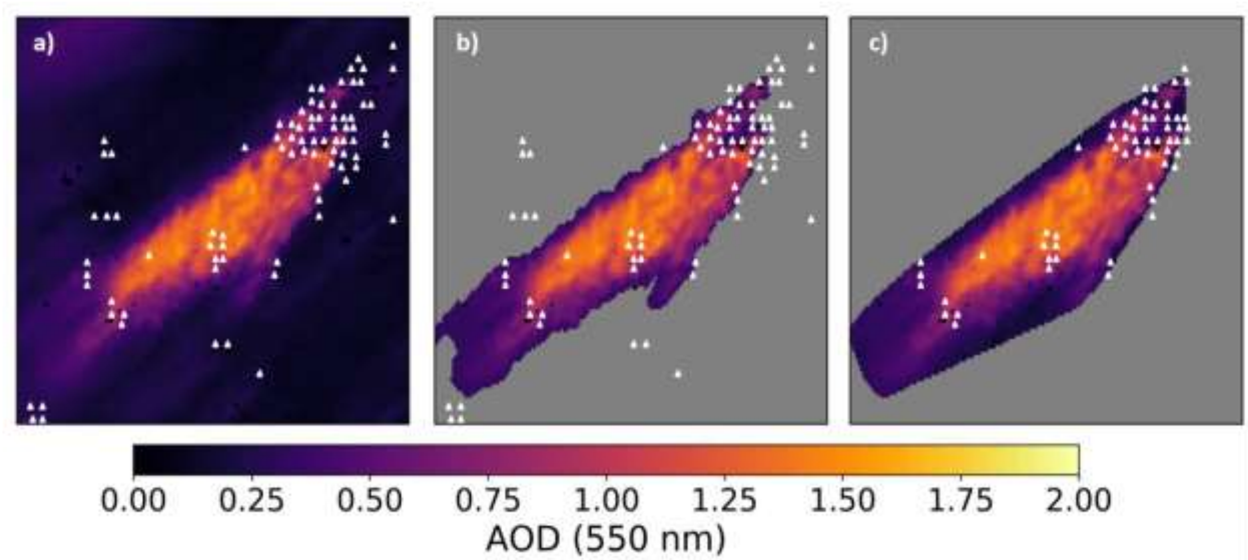

(2 column) **Figure 4.** Example region of interest (ROI) containing the fire shown in Figure 1 along with matchup active fire pixels (*white triangles*) from the Meteosat FRP-PIXEL product detected between midnight and the MODIS overpass time. (a) MAIAC 1km AOD and SEVIRI active fire (AF) pixels; (b) histogram thresholding to discriminate the plume from the surrounding 'ambient' background. (c) SEVIRI AF pixels detected within the convex hull of the plume are considered to come from the same 'fire' that produced the smoke plume. The fire radiative energy (FRE) of the causal fire is then calculated from these observations and used to match to the AOD-derived total particulate matter (TPM) (see Figure 5).

Following Mota and Wooster (2018), only fire matchups for which a single FREMv2 biome represented more than 50% of the observed FRP pixels in a fire were retained. In some cases, the MAIAC AOD cloud mask did screen out some pixels within the smoke plume (e.g. Fig. 1d), though the impact was far less than for the 10 km MODIS MxD04 AOD data. To preserve the accuracy of fire emitted TPM estimates, matchup fires were limited to those with plumes having a MAIAC AOD retrieval at more than 95% of their pixels, and radial bias function interpolation was used to interpolate over the relatively few missing AOD values. To assess the impact of this interpolation on the calculated TPM values, we purposely removed additional AOD pixels and re-estimated their value via the same process. Minimal impact was shown due to the quality of the interpolation procedure and the fewer than 5% of in-plume AOD pixels it was required to be applied to.

After pre-processing and data screening, 968 fire matchups remained for C_{biome} derivation, and these are mapped in Figure 6d. Each had its FRE and column integrated mass of total plume particulate matter estimated, the former from the temporal integration of FRP from the start of fire activity on that day to the time the MAIAC AOD data were acquired. The latter was calculated from the plumes' total plume AOD anomaly divided by the smoke aerosol mass extinction coefficient, β_e (in $m^2.g^{-1}$) and multiplied by the total plume area (m^2) calculated over all AOD pixels (following Ichoku and Kaufman, 2005). β_e can be measured *in situ* and its value depends on several factors including relative humidity, age of the smoke, vegetation burned and the wavelength used in measurements. Reid et al. (2005) provide a detailed review of values for β_e in smoke plumes that range between 3.8 - 4.5 $m^2.g^{-}1$, and combining these with the values of Abel et al. (2005) for South African fires that range from 2.22 – 3.37 $m^2.g^{-}1$ we assume an intermediary β_e of 3.5±1.0 $m^2.g^{-1}$. β_e values for smoke have been shown to increase with aerosol ageing (Formenti et al., 2003; Abel et al., 2005) and also with relative humidity (RH) (Chin et al., 2002; Koppmann et al., 2005). The RH for each of our plumes was taken from the ERA-Interim reanalysis at 762 m altitude (Balsamo et al., 2015), and all matchup plumes showed coincident RH values < 70% so we assume minimal effect of RH on β_e since below this RH threshold inflation of β_e for smoke generated from biomass burning is typically less than 10% (Chin et al., 2002; Reid et al., 2005). The β_e of fresh smoke aerosol has been shown to increase by 20 to 50% as it ages after 1 - 4 days (Reid et al., 1998; Abel et al., 2005). However, for the majority of our fire matchups, significant fire activity was not observed until 08:00 hrs or later in the day, resulting in the oldest smoke in our plumes being around 7 or 8 hours old and thus limiting the extent to which β_e grows due to plume ageing. We therefore retain the β_e value of 3.5±1.0 $m^2.g^{-1}$ used by Mota and Wooster (2018), and the uncertainty range attached to this value also includes these potentially higher bounds. We do however recommend further investigation into the potential for biome-dependent variability in β_e.

4.3 Derivation of Smoke Emission Coefficients (C_{biome})

Our fire matchups were used to derive a set of smoke emission coefficients (Table 1; Fig. 5) for each of the biomes defined in Section 4.1, based on zero-intercept linear orthogonal distance regression (ODR). Uncertainties in each variable are accounted for in ODR and are calculated from the combined AOD uncertainty measures provided in the MAIAC product, the uncertainty in β_e, and the FRP uncertainties provided in the FRP-PIXEL product (Wooster et al., 2015).

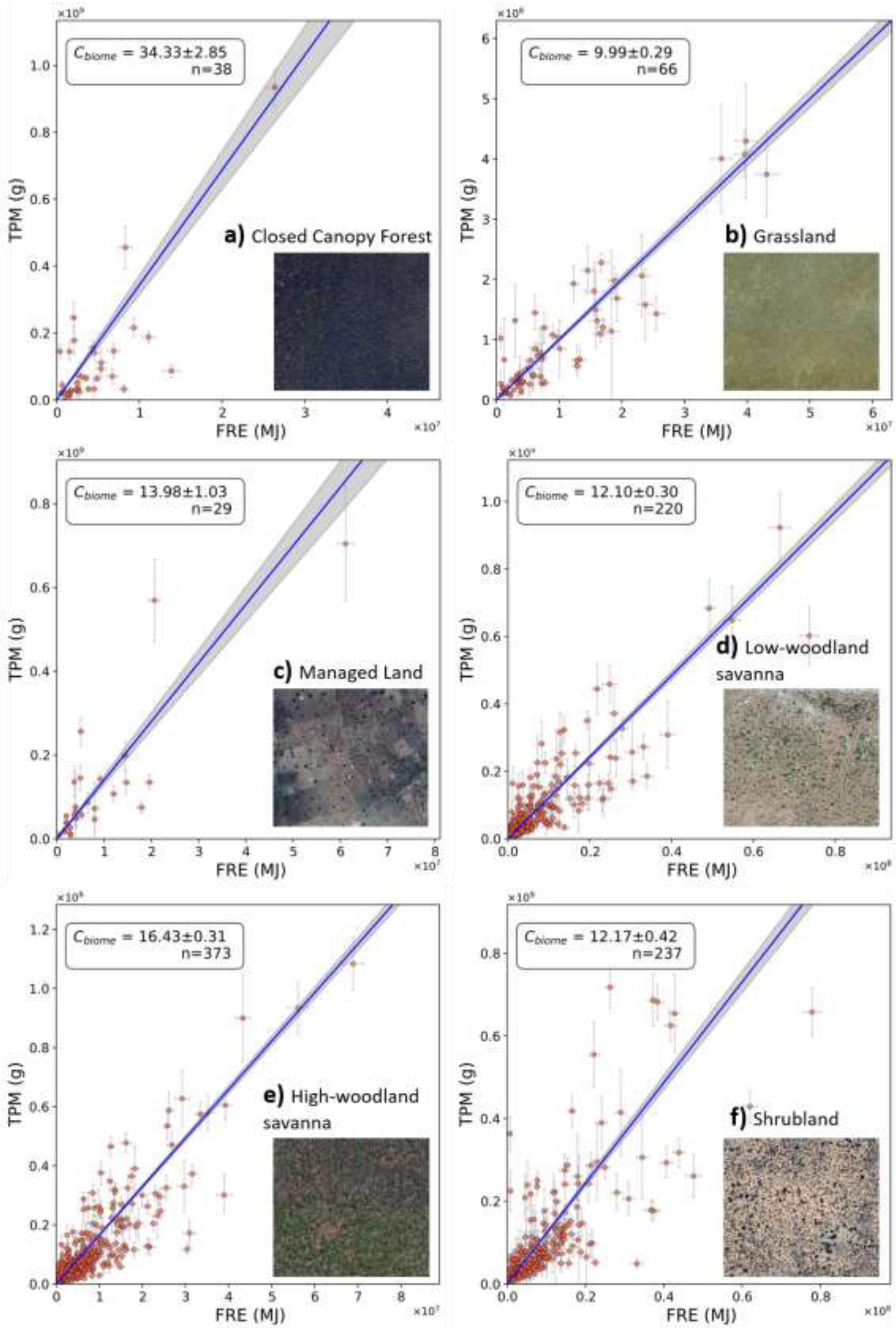
C_{biome} = 34.33±2.85
n=38
a) Closed Canopy Forest
C_{biome} = 9.99±0.29
n=66
b) Grassland
C_{biome} = 13.98±1.03
n=29
c) Managed Land
C_{biome} = 12.10±0.30
n=220
d) Low-woodland savanna
C_{biome} = 16.43±0.31
n=373
e) High-woodland savanna
C_{biome} = 12.17±0.42
n=237
f) Shrubland
TPM (g)
FRE (MJ)

(2

column) **Figure 5.** Smoke emission coefficients (C_{biome}; in g.MJ^{-1}) for the six African fire-affected biomes defined in Section 4.1, each derived from the slope of an orthogonal distance regression (ODR) between data on fire-emitted total particulate matter (TPM) and matching fire radiative energy (FRE). Grey shaded area defines the 95% probability prediction interval of the ODR-derived slope. Each scatterplot is accompanied by an illustrative insert that depicts the typical landcover for the biome as seen in Google Earth (example locations are Closed Canopy Forest, 10.359° S, 19.086° E; Grassland 21.180° S, 19.560° E; Managed Land 10.495° N, 7.586° E; Low-Woodland Savanna 7.085° N, 27.095° E, High-Woodland Savanna 12.523° S, 23.323° E; Shrubland 23.055° N, 22.242° E).

Table 1. Biome-dependent smoke emission coefficients (C_{biome}) and accompanying uncertainties for the African fire-affected biomes mapped in Figure 3b and calculated from FREMv2 and from FREMv1 (reported in Mota and Wooster (2018)). Matching FEER-equivalent coefficients are also shown, based on the geographical location of fire matchups and the FEER Ce (1° × 1°) product of Ichoku and Ellison (2014).

Biome	FREMv2 C_{biome} (g MJ^{-1})	FREMv1 C_{biome} (g MJ^{-1})	FEER equivalent C_{biome} (g MJ^{-1})
Closed canopy Forest	34.33±2.85	65.63±0.91	16.34
Managed land	13.98±1.03	15.62±0.34	15.80
Grassland	9.99±0.29	13.03±0.23	10.98
Shrubland	12.17±0.42	17.36±1.06	10.97
Low-woodland savanna	12.10±0.30	19.75±0.49	12.78
High-woodland savanna	16.43±0.32	19.75±0.49	13.81

Our FREMv2 smoke emission coefficients were compared to those of FREMv1 (Mota and Wooster, 2018) and FEER (Ichoku and Ellison, 2014; Table 1). In FEER, C_e values are derived for each individual 1˚ grid cell using the MODIS archive of that cell, rather than by biome. To derive FEER-equivalent C_{biome} values for comparison, we intersected all FREMv2 fire matchups with each FEER 1˚ grid cell and then calculated the mean FEER C_e for each of our biomes.

Our FREMv2 C_{biome} values range from 9.99 ± 0.29 g MJ^{-1} (grassland) to 34.33 ± 2.85 g MJ^{-1} (closed canopy forest), and in all biomes are lower than those of FREMv1 with an average decrease of 27% across all biomes, that for closed canopy forest is almost halved compared to FREMv1. These differences relate to a combination of the far more appropriate MAIAC AOD product, the improved method for background AOD estimation, the updated and extended biome mapping, and the inclusion of fire matchups from NHAf as well as SHAf. Since plume TPM values are most strongly influenced by the AOD product used, use of MAIAC AODs is likely to have the most significant impact on the C_{biome} values and the product characteristics can both increase and decrease these compared to use of MxD04. As discussed in Sections 2.3 and Section 3, MxD04 AOD retrievals are VZA dependent and bias can be seen at the swath edges (Sayer et al., 2015), meaning TPM estimates for plumes observed at wide VZA can be significantly inflated (Fig. 2a). In the original FREMv1 methodology such plumes were retained during the C_{biome} derivation, and likely resulted in overestimated TPM values and thus FREMv1 C_{biome} values. Additionally, the MAIAC AOD product uses an area-weighted method to grid L1B MODIS pixels to a 1 km pixel size prior to AOD retrieval, providing finer detail and improved plume distinction at VZA > 20°, allowing inclusion of smaller fires in the matchup dataset. A feature of the MAIAC AOD product likely to increase estimates of TPM and thus FREMv2 C_{biome} values is its less conservative cloud mask, which resulted in MAIAC-derived TPM estimates being ~ 26% higher than the equivalent MxD04_BD values when only plumes observed at low VZA's are considered (Fig. 2b).

Final C_{biome} values for shrubland and low-woodland savanna are close (within 0.07 g MJ^{-1}) (Table 1), indicating these biomes appear broadly equivalent with respect to their fire and particulate matter emissions characteristics. The number of fire matchups identified in both the closed canopy forest and managed land biomes are significantly fewer than for the other biomes, largely because of fewer identifiable fires and the fact that many do not meet the matchup criteria. The lower number of matchups mean the C_{biome} coefficients for these two biomes have significantly larger uncertainties (3× and 10× higher than for the other biomes respectively), and their smoke emissions coefficients are quite strongly influenced by a relatively few high FRE fire matchups. As discussed in Section 2.1, the SEVIRI FRP-PIXEL product has a minimum AF detection limit of around 30 - 40 MW, and fires burning below this will often remain undetected until they breach this threshold or other fires within the same pixel cause the pixels FRP total to exceed this. Agricultural fires in managed lands are typically quite small (Zhang et al., 2017), and in closed canopy forests surface fires burning on the forest floor will be partially obscured by the tree canopy (Roberts et al., 2018a). Both these effects will result in a lower FRE total being measured at a fire than might otherwise be the case, and these biomes also have the highest percentage of matchups with FRE below 1×10^7 MJ. But to the extent that these issues affect both the matchup fires of these biomes and the overall set of SEVIRI-detected fires to which the coefficients are applied, the effect of these issues is taken into account. FREMv2 coefficients are on average only 18% higher than FEER-equivalent C_{biome} values, with FREMv2 $C_{low-woodland\ savanna}$ (which has one of the largest matchup sample sizes) showing very good agreement with its FEER- equivalent (12.10±0.32 and 12.78 g MJ^{-1} respectively). FREMv2 $C_{low-woodland\ savanna}$, $C_{shubland}$ and $C_{grassland}$ values are also all within 11% of their FEER-equivalents. $C_{closed\ canopy\ forest}$ shows the greatest divergence at around twice the FEER-equivalent, perhaps stemming from the relatively small sample size (n=38) and/or the high variability in FEER C_e values for this biome (Fig. 6b).

The newly derived FREMv2 C_{biome} values of Table 1 were used to generate a SEVIRI per-pixel smoke emissions coefficient (C_e) product for Africa, for subsequent use in smoke emissions estimation. C_e values for each SEVIRI pixel across the African continent were calculated based on the weighted mean of the relevant C_{biome} values and the per-pixel biome fractional cover derived in Section 4.1. Figure 6a shows the resulting FREMv2 C_e product, along with the FEER C_e (1° × 1°) product (Ichoku and Ellison, 2014) (Fig 6b) and their difference (averaged to 1˚ resolution) (Fig. 6c). As previously described, FEER C_e values are calculated for each 1˚ grid cell from matchup fires within that cell, rather than per biome, so the spatial variability of FEER C_e values is far higher than for the biome-driven FREMv2 C_e values of Fig. 6a. Across Africa, FEER C_e are on average higher than those of FREMv2 by 0.53 g.MJ^{-1}, and this difference is dominated by regions where the FEER coefficient is significantly higher than that of FREMv2 (Fig. 6c). The most similar regions are generally those well sampled by fire matchups in FREMv2 (Fig. 6d), whereas those with the highest differences have few or no fire matchups in FREMv2, due primarily to relatively low fire activity being recorded there but also frequent cloud cover in 2015. In some cases such areas appear to exhibit notably high FEER C_e values (> 40 g.MJ^{-1}). Future work on

FREM will extend the fire matchup sampling period to multiple years to obtain additional matchups in regions currently relatively poorly sampled, and will aim to better understand the large divergence in C_e values compared to FEER in these locations.

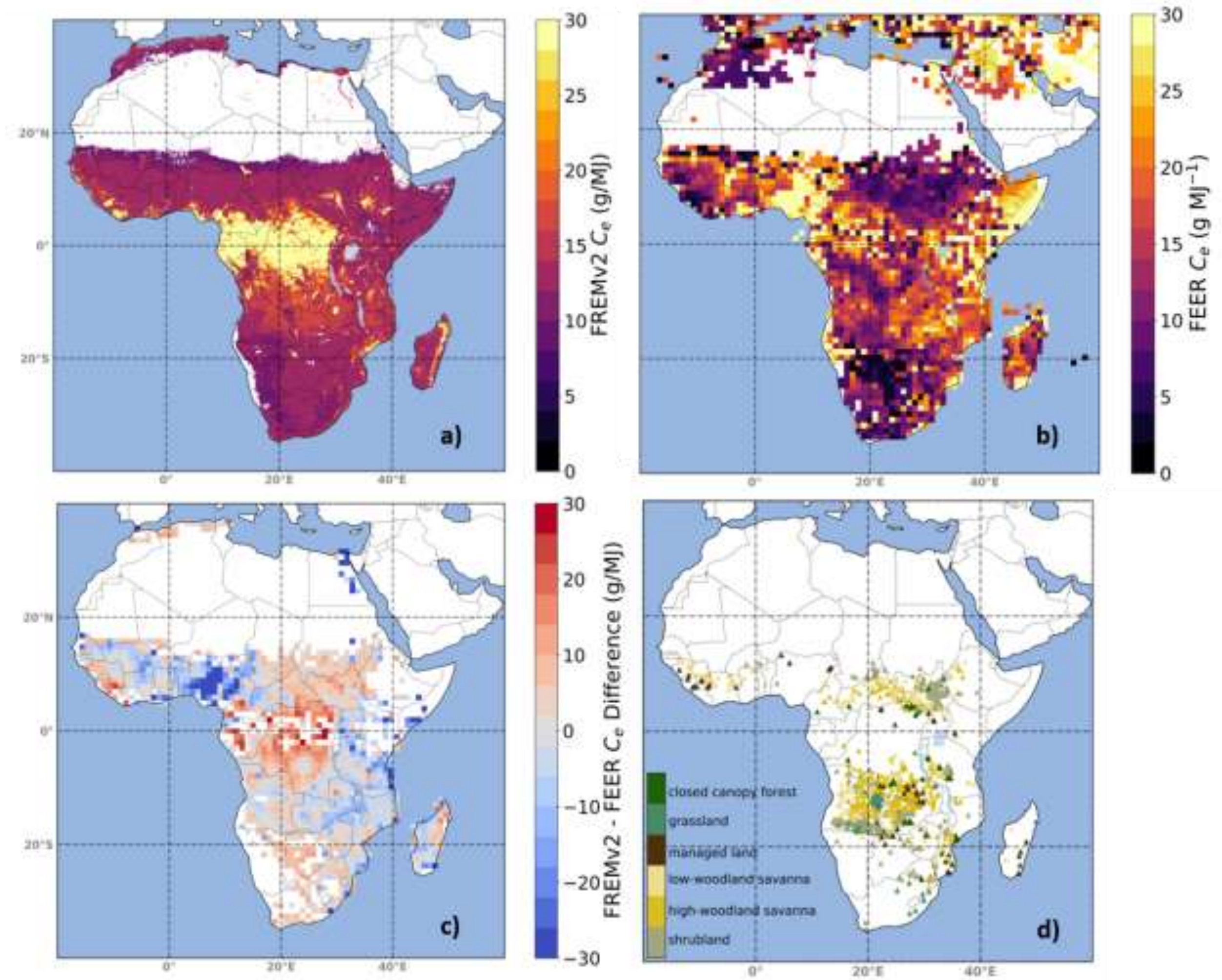

(2 columns) **Figure 6.** (a) FREMv2 smoke emission coefficient (C_e) mapped at 0.05˚; (b) the matching 1˚ FEER C_e product; and (c) the difference. In (c), FEER grid cells whose value was derived from gap-filling or which were calculated from less than 15 samples were removed (see Ichoku and Ellison (2014) for full details). (d) Shows the spatial distribution of the fire matchups used to derive the FREMv2 C_{biome} values of Figure 5.

5. FREMV2 EMISSION INVENTORY DEVELOPMENT

5.1 Total Particulate Matter (TPM) Emissions

We used the FREMv2 C_e product of Figure 6a to convert the 2013 to 2018 Meteosat FRP-PIXEL product (Wooster et al., 2015) into the highest spatio-temporal resolution TPM emissions inventory yet available over Africa (15 min, 3 km at the sub-satellite point). We compared these emissions to a series of other inventories widely used by the research and operational communities (Figs. 9 and 10). Hourly averages of SEVIRI FRP (in MW) multiplied directly by the FREMv2 C_e product provide mapped instantaneous TPM emission rates (in $kg.s^{-1}$), whereas multiplication by FRE gives emission totals for the defined FRP temporal integration period. Figure 7 presents TPM emissions estimates for FREMv2, GFASv1.2 (Kaiser et al., 2012; https://apps.ecmwf.int/datasets/data/cams-gfas/), GFEDv4.1s (Van der Werf et al., 2017; www.globalfiredata.org/), along with FEERv1.0-GFAS1.2 (the FEER C_e product applied to GFASv1.2 FRP estimates, Ichoku and Ellison, 2014; www.feer.gsfc.nasa.gov/data/emissions/) and FEERv1.0-SEVIRI (the FEER C_e product applied to SEVIRI FRE).

FREMv2 estimates mean annual TPM emissions for Africa at 32.41±1.86 $Tg.yr^{-1}$ for the five years studied, 38% of which are generated from fires in NHAf, and 62% SHAf. Pan-African totals are 114% and 69% higher than GFASv1.2 and GFEDv4.1s respectively, with estimates from SHAf fires showing greater divergence in both cases. The FREMv2 values however, are within 11% of the top-down inventories FEER-GFASv1.2 and FEER-SEVIRI, agreeing with Ichoku and Ellison (2014) who also show FEER-GFAS to be higher than GFASv1 and GFEDv3 by similar factors over NHAf and SHAf. Kaiser et al. (2012) report that GFASv1.2 smoke aerosol emissions must be multiplied by a global scaling factor of 3.4 before input into atmospheric models if they are to provide modelled AODs more in line with observations. This provides evidence that Africa's TPM emissions are indeed higher than GFAS (and GFED) currently estimate. As demonstrated by

Wooster et al. (2015) and Hall et al. (2019), at the time of their overpasses, polar-orbiter based AF products detect more "small" (i.e. low FRP) fires compared to the SEVIRI FRP-PIXEL product as a result of their finer pixel size and thus lower minimum FRP detection limit. This effect is amplified at SEVIRI VZA > 40° due to the growth of sensors pixel footprint area. However, it was also shown that over the course of several days, the far more frequent data available from SEVIRI allows an increased number of AF detections overall (Wooster et al., 2015; Hall et al., 2019). Since the SEVIRI-derived FREMv2 emissions agree well with those of FEER, which are derived from MODIS FRP data (which have a significantly lower minimum FRP detection limit than SEVIRI; Roberts et al., 2015), our findings suggest that FREMv2 accounts for the smoke emission contribution from a substantial proportion of the active fire pixels remaining undetected by SEVIRI. This is likely because, whilst SEVIRI fails to detect these lowest FRP fires, the smoke they generate has contributed to the AOD in the 1km MAIAC product used to generate the biome-dependent smoke emissions coefficients from the fire matchups. Thus, our FREMv2 C_{biome} and C_e data contain an inherent 'boost' from the TPM emitted from undetected low-FRP active fire pixels. The 1 km spatial resolution of the MAIAC AOD, which enables us to distinguish and use many more of the smaller smoke plumes than the higher resolution MxD04 product, helps enable this compared to the 10 km AOD data used in FREMv1.

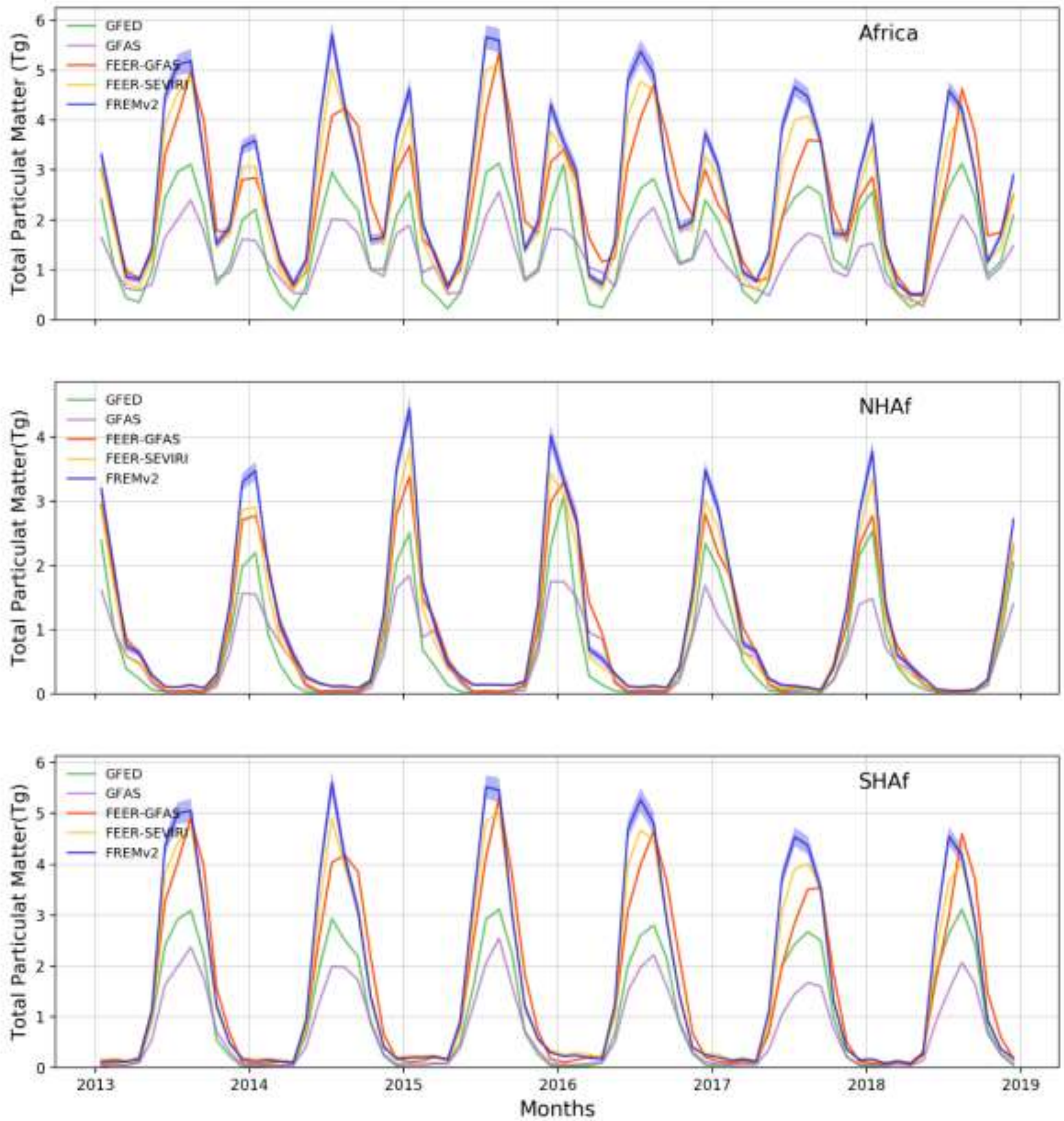

(2 columns) **Figure 7.** Monthly total particulate matter (TPM) emissions from landscape fires for 2013 to 2018, as derived using the FREMv2 methodology *(blue)* applied to the Meteosat FRP-PIXEL product of Wooster et al. (2015). Corresponding monthly TPM emissions are shown from GFEDv4.1s *(green)*, GFASv1.2 *(purple)*, and the FEERv1.0 coefficients applied to the GFASv1.2 *(red)* and SEVIRI FRE data *(yellow)*.

The five inventories of Figure 7 show similar temporal patterns of TPM emission, with clearly identifiable NHAf and SHAf burning seasons and annual peaks and minima occurring in the same years. Like Mota and Wooster (2018), FREMv2 predicts an earlier peak in TPM emissions over SHAf than do the other inventories. Peak smoke emission in FREMv2 occurs in July in every year but one, whereas in all other inventories (except FEER-SEVIRI, which has peak TPM split equally between July and August) this occurs in August. A potential cause may be the splitting of high and low woodland savanna biomes in FREMv2. High-woodland savanna is mainly concentrated just below the equator (Fig. 3b), in a region that burns far earlier than the dominant southern African fire season. Therefore, due to FREMv2 discriminating between high and low woodland savanna and grasslands, the dominant C_e values applied to the SEVIRI FRP-PIXEL data vary not only by biome, but also over time due to the seasonal progression of fire activity across the continent. Due to the FREMv2 biome map being based on land cover and VCF data from 2015, changes in land cover in the 2013 to 2018 period are not accounted for. However, canopy changing crown fires are very rare in low and high-woodland savanna, shrublands and grasslands – which are dominated by surface fires (Van Wilgen et al., 1990; Heil et al., 2010; Van Leeuwen et al., 2014) - and so fire-related changes in tree canopy cover is very limited in these biomes (Zhou et al., 2019). However, year-to-year anthropogenically driven landcover changes could impact the methodology and it may become more important to account for such changes within our FREMv2 coefficients as this increases. Future FREM versions will include more regular landcover updates in the mapped emissions coefficient estimation.

The similar TPM estimates generated by FEER-GFASv1.2 (which uses MODIS FRP) and FEER-SEVIRI (and FREMv2, which both use SEVIRI FRP), compared to the far lower values of GFASv1.2 (also based on MODIS FRP) indicate that the higher TPM emissions of the top-down approaches stem dominantly from the C_e values applied to FRP measures, and less so from the source of the FRP observations used. That said, in the case of FEER-GFASv1.2 it is noteworthy that whilst the FEER C_e values are derived from use of direct MODIS FRP observations, the MODIS FRP data used within GFAS undergoes several stages of processing and thus presents different FRP values to those originally provided by the MODIS MOD14/MYD14 products (Kaiser et al., 2012). The similarity of the TPM emissions estimates generated by FREMv2 and the two FEER inventories supports the case that higher emissions estimates come mainly from the magnitude of C_e values, since the FREMv2 and FEER C_e values agree well in general (Table 1 and Fig. 8). Future work will evaluate the quality of the final TPM emissions generated by FREMv2 by placing them as inputs to atmospheric chemical transport models and comparing the resulting aerosol fields to independent data such as AERONET and surface $PM_{2.5}$ measures.

We generate 2016 FREMv2 TPM emissions at 0.05˚ across the African continent, a spatial resolution ×5, ×2 and ×2 times higher than offered by GFEDv4.1s, GFASv1.2 and FEER-GFASv1.2 respectively. We present these for Africa along with a magnified 20×20˚ region in Figure 8. The FEER C_e product with its 1˚ grid cell resolution can, in theory, be applied to the native SEVIRI FRP-PIXEL product as has been done for the FEER-SEVIRI dataset shown in Figure 8. However, the spatial resolution of the FEER C_e product is 20 times lower than that of the FRP observations, so these FEER-SEVIRI derived emissions estimates do not account for the finer detail inter-biome spatial variations that FREMv2 does. Additionally, the appropriateness of applying FEER C_e values, which are derived from 'raw' MODIS FRP data, to 'raw' SEVIRI FRP data is unclear, particularly when their quite different minimum-FRP detection limits are considered.

In general, the spatial distribution of the African TPM emissions is somewhat similar across all five inventories. In line with the temporal trends of Fig. 7, we see notably higher TPM totals for the three top-down emission inventories, particularly FREMv2. The high spatial resolution of

FREMv2 provides more precisely detailed spatial information on smoke emissions than do the other inventories, which maybe relevant for supporting improved local scale air quality modelling. In FREMv2, deriving separate C_{biome} coefficients for high- and low-woodland savanna results in distinctly higher total TPM emissions in north Angola/south D.R.C. compared to the other inventories. This region is dominated by high-woodland savanna (Fig. 3b), and demonstrates the impact of the more spatially resolved biome classification used in FREMv2.

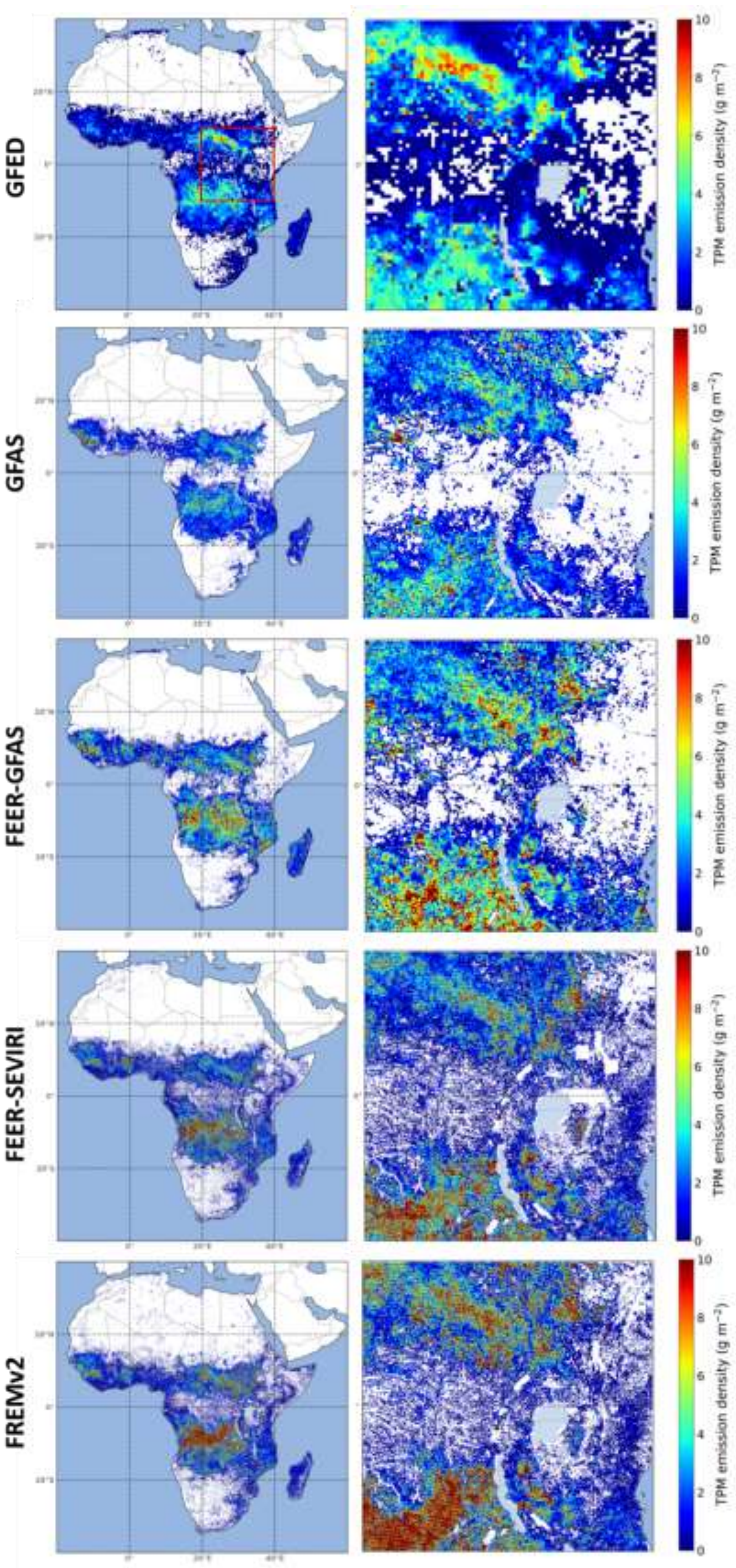
GFED
GFAS
FEER-GFAS
FEER-SEVIRI
FREMv2
TPM emission density (g m^{-2})

(1.5 columns) **Figure 8.** Total particulate matter (TPM) emission density (g.m^{-2}) across Africa for 2016 as determined by GFEDv4.1s (0.25° grid cells), GFASv1.2 (0.1° grid cells), FEERv1.0-GFASv1.2 (0.1° grid cells), FEERv1.0-SEVIRI (0.05° grid cells), and FREMv2 inventory derived herein (0.05° grid cells). The red 20° × 20° region outlined in the top left GFED plot is shown magnified for each inventory in the right-hand column.

The distribution of biomes across NHAf and SHAf has a significant impact on the contribution each biome has to the total TPM emissions of each hemisphere (Fig. 9). Both closed canopy forest and grassland show a similar percentage contribution to total TPM emissions in each hemisphere, with mean annual emissions totals within 2% of each other and a combined mean contribution of 17% and 20% of total TPM emissions for NHAf and SHAf respectively. In NHAf, fires from managed lands and shrublands contribute most to annual TPM emissions, though their fractional contributions exhibit significant seasonal variations (45% and 38% across the year respectively). In SHAf these two biomes show a narrower range across the year and an overall lower contribution to total TPM emissions, which are instead dominated by high-woodland savanna fires between May and November. In both NHAf and SHAf, the highest monthly contribution of emissions from managed lands occurs outside the primary burning season (Nov-April in NHAf and July-Sept in SHAf), potentially due to deliberate post-harvest or end-of-growing season burning (Yevich and Logan, 2003).

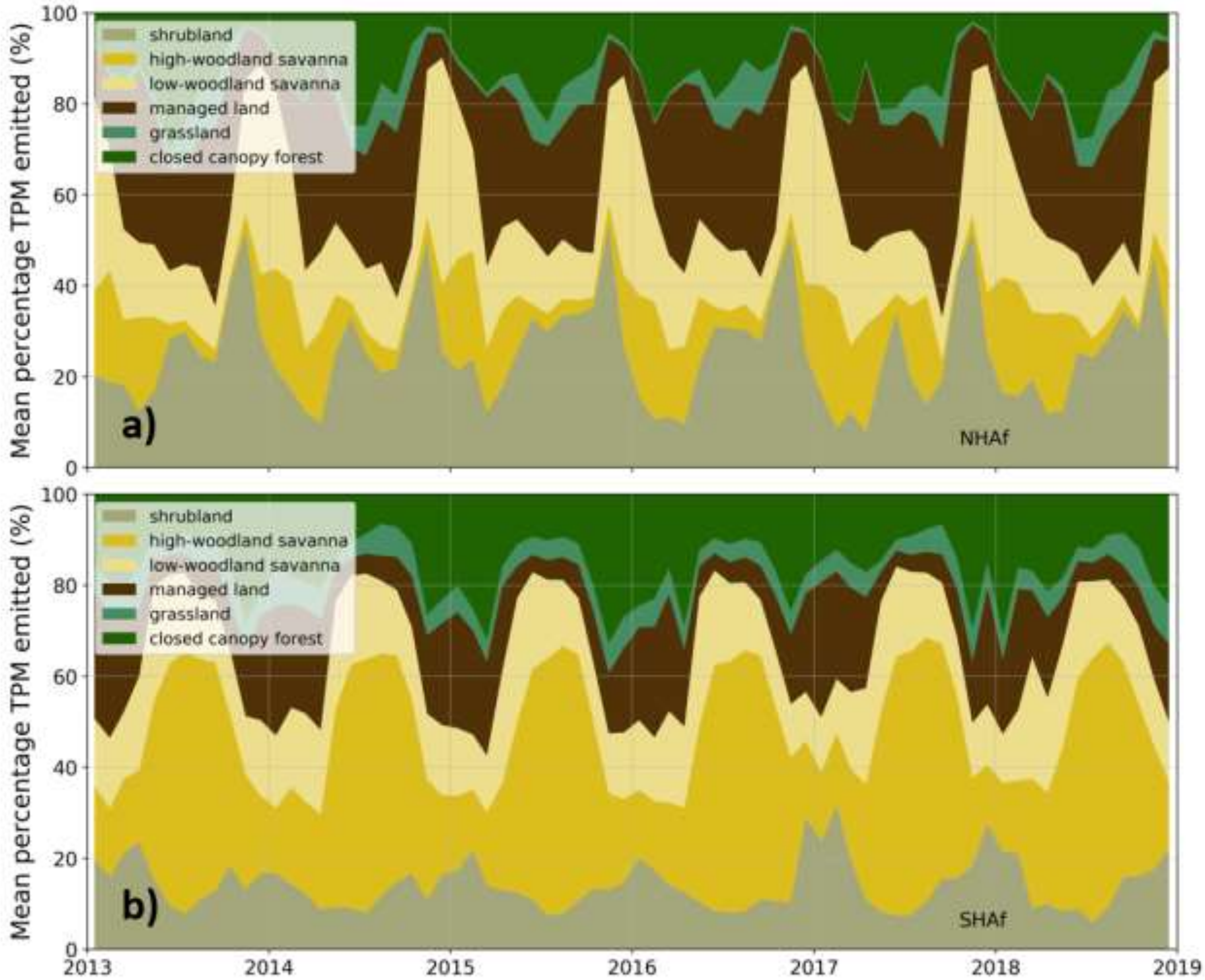

(1.5 columns) **Figure 9.** Mean monthly contribution (%) of fires to total particulate matter (TPM) emissions in each of the six FREMv2 biomes from 2013 to 2018 in (a) Northern Hemisphere Africa and (b) Southern Hemisphere Africa.

5.2 Trace gas and total carbon emissions

As with FREMv1 (Mota and Wooster, 2018), trace gas emissions estimates are derived from FREMv2 outputs via application of the standard gaseous emission factors (EFs) of Andreae and Merlet (2001), which are also used in GFEDv4.1s, GFASv1.2 and FREMv1. Although EF updates to Andreae and Merlet (2001) have recently become available (Andreae, 2019), we maintain the use of the original EFs for consistency and ease of comparison with the other fire emissions databases. Unlike the bottom-up approaches in which the EFs are applied to total fuel consumption estimates, in the FREM methodology trace gas emissions are estimated directly from the observed FRP or FRE values using a set of trace gas emissions coefficients. The approach is similar to that of Huijnen et al. (2016) who estimated CO_2 and CH_4 emissions from fire-emitted CO estimates. The trace gas emission coefficients in FREM are calculated using the EF ratios between the relevant gas and TPM, which are then multiplied by the TPM C_{biome} values presented in Section 4.4 (Table 1) (Mota and Wooster, 2018):

$$C_{gas}^{biome}\ [\,g.MJ^{-1}] = \frac{EF_{gas}^{biome}\ [g.kg^{\ -1}]}{EF_{TPM}^{biome}\ [g.kg^{\ -1}]} \cdot C_{TPM}^{biome}\ [g.MJ^{-1}]$$

These coefficients are applied directly to the geostationary FRP or FRE data to estimate the trace gas emissions. Trace gas emissions coefficient derivation for each SEVIRI pixel used an area-weighted mean of the biome-specific EF ratios (similarly to C_e product derivation in Section 4.3), thereby generating an emission coefficient map for each gas. The biomes used by Andreae and Merlet (2001) to report their EF values are less detailed than those of FREMv2, resulting in all but the closed canopy forest biome using the same EF values. This relative lack of EF detail affects all the fire emission inventories compared herein, and points to a potential need for more research focused on more finely detailed EFs with respect to vegetation type.

Final monthly CO_2, CH_4 and CO emissions are shown in Figure 10, which exhibit a similar seasonal pattern to those of TPM (Fig. 7), and mean annual totals are shown in Table 2. Direct retrieval of CO atmospheric concentrations is carried out using data from instruments such as MOPITT (Worden et al., 2010) and TROPOMI (Veefkind et al., 2012), and comparisons of GFEDv2 and GFEDv3 CO emissions with MOPITT-derived CO have previously suggested that GFED underestimates fire emitted CO over Africa by up to 50% (Chevallier et al., 2009; Kopacz et al., 2010; Pechony et al., 2013). Comparisons of the different GFED versions shows that for NHAf and SHAf, GFEDv4.1s CO emissions were around 30% lower than GFEDv3 (Van Der Werf et al., 2017), pointing to significant underestimation of CO emissions by GFEDv4.1s over Africa, similarly to that of TPM. Studies showing African burned area to be far higher when mapped using 20 m Sentinel-2 MSI imagery than with the 500 m MCD64A1 product used in GFED supports this idea (Tsela et al., 2014; Hawbaker et al., 2017; Roteta et al., 2019). The substantially higher CO emissions provided by FREMv2 and by the other top down approaches compared herein may therefore be more realistic than the lower values provided by the bottom up inventories.

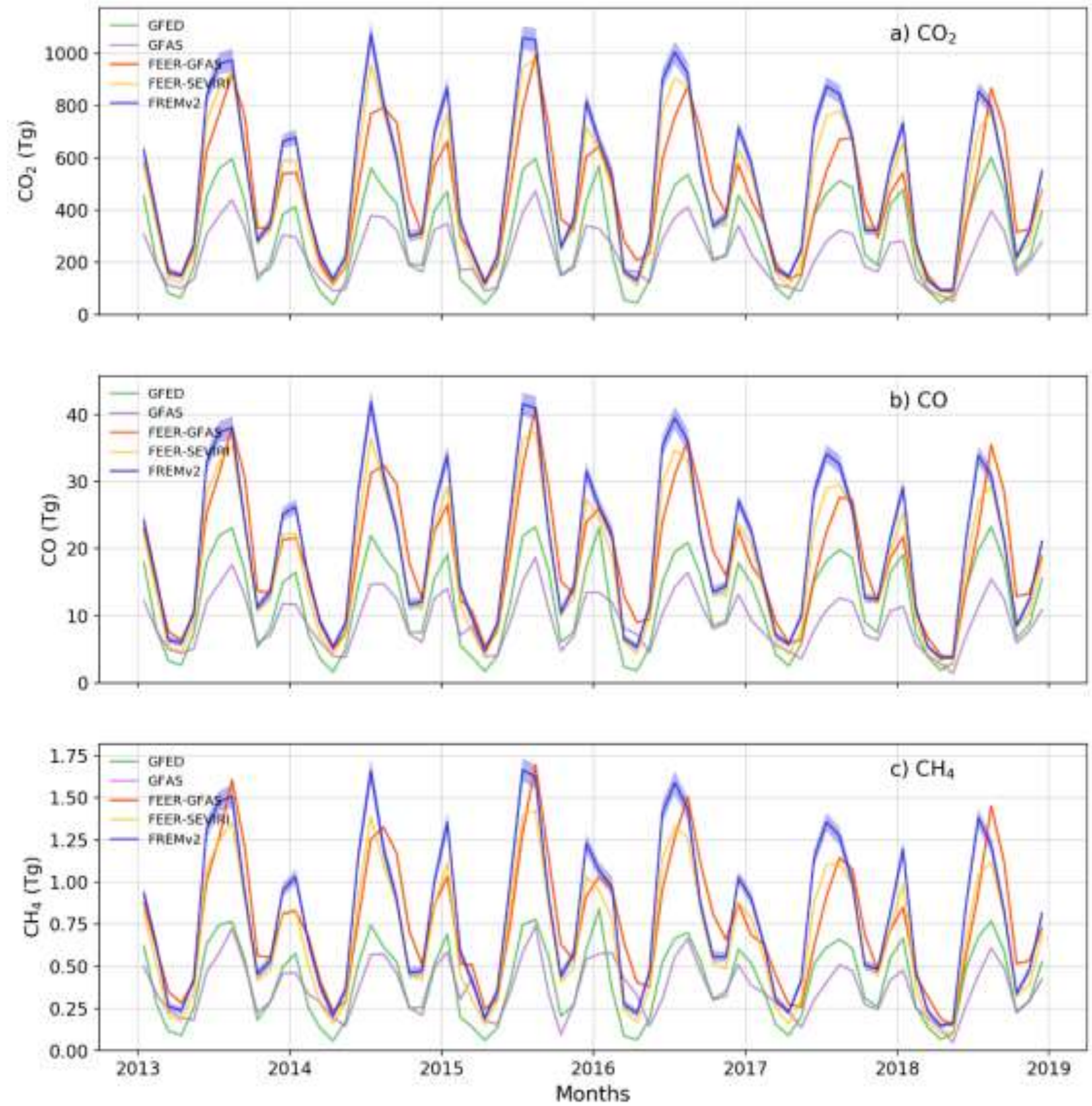

(2 columns) **Figure 10.** Monthly total emissions (Tg) of (a) CO_2; (b) CO; and (c) CH_4 for African landscape fires as estimated by FREMv2 (*blue*) between 2013 and 2018. Corresponding values from GFEDv4.1s (*green*), GFASv1.2 (*purple*), FEERv1.0-GFASv1.2 (*red*) and FEERv1.0-SEVIRI (*yellow*) are shown for comparison.

FREMv2 emissions of total carbon were calculated from the summed carbon contents of the CO_2, CO and CH_4 emissions, which typically contribute more than 99% of total carbon release in savanna/grassland and tropical forest fires (Andreae, 2019). Estimates of total fuel consumption in terms of dry matter consumed (DMC) were then calculated on the assumption of a 50% DM fuel carbon content (Van Der Werf et al., 2010; 2017), with mean annual totals reported in Table 2.

Table 2. Mean annual total carbon and trace gas emissions for 2013 to 2018, along with dry matter consumed (DMC) totals (Tg.yr^{-1}), for Northern and Southern Hemisphere Africa as estimated by the different fire emissions inventories compared herein including FREMv2 (final column).

	Mean annual emissions (Tg yr^{-1})									
	GFAS		GFED		FEER-GFAS		FEER-SEVIRI		FREMv2	
Species	NHAf	SHAf	NHAf	SHAf	NHAf	SHAf	NHAf	SHAf	NHAf	SHAf
C	346.3	470.3	398.1	651.4	588.3	1007	593.5	1023	682.7±76.9	1090±46
CO_2	1188	1619	1368	2242	2018	3457	2045	3525	2349±270	3751±167
CO	48.25	62.87	54.74	87.62	82.54	141.03	77.94	134.8	91.52+10.53	147.1±6.6
CH_4	2.033	2.421	1.921	2.953	3.375	5.708	2.966	5.164	3.623±0.417	5.894±0.263
Dry Matter Consumed	692.6	940.6	796.2	1302.8	1176.6	2014	1187	2046	1365±154	2180±92

5.3 Fuel Consumption per unit area (F_c) from 20 m Burnt Area

As discussed in Section 2.1, poorly constrained fuel load and combustion completeness parameters contribute a significant part of the uncertainty in bottom up estimates of fuel consumption per unit area (F_c, in kg.m^{-2}), and unmapped small burns missed by the 500 m

MCD64A1 MODIS burned area (BA) product adds further uncertainty and possibly bias into the final derived fuel consumptions (Reid et al., 2009; Vermote et al., 2009; Van Leeuwen and Van Der Werf, 2011; Tsela et al., 2014; Hawbaker et al., 2017; Roteta et al., 2019). As first demonstrated by Mota and Wooster (2018), it is however possible to generate FREM-derived estimates of F_c through an inversion of the original Seiler and Crutzen (1980) BA-based approach to fire carbon emissions estimation. The 500 m MODIS MCD64A1 BA product used in GFED (Van Der Werf et al., 2017) and in the calibration of GFAS (Kaiser et al., 2012) was used in mapping of F_c across southern Africa in FREMv1 (Mota and Wooster, 2018), but here we use the far higher spatial resolution (20 m) FireCCISFD11 African BA product for 2016 that has been shown to map up to 60% more BA in some areas through the detection of far smaller burn patches (Roteta et al., 2019). We mapped F_c across Africa at 0.25° (Fig. 11a) by gridding the FREMv2 dry matter consumed (DMC) data for 2016 (Section 5.2) and dividing this by the matching BA calculated from the approximately 1.5×10^6 potential FireCCISFD11 20 m pixels falling in each 0.25° grid cell. Note that these per-pixel F_c values apply only to the burned area patch inside a given pixel, and not the 0.25° pixel as a whole. Compared to F_c provided by the model-based GFEDv4.1s (Figure 11b), around half the grid cells show a significantly higher F_c value in FREMv2, which is to be expected due to the overall higher carbon emissions of the former (Fig. 10 and Table 2), and for the remaining cells the two inventories provide similar values (see difference map in Appendix C). There are some unprocessed tiles in the FireCCISFD11 product (see Roteta et al. (2019)), resulting in a small minority of 0.25° grid cells having unreported or unrealistically high F_c values in excess of 10 $kg.m^{-2}$. Avoiding use of these few anomalous cells, we derived biome-specific F_c frequency distributions and statistics based on those cells where the biome covered at least 80% of the cell area and where more than 5% of the cell burned (Figure 11c). Distributions are heavy-tailed and show a spatial variability somewhat similar to that derived by Roberts et al. (2011) using an alternative FRE and BA based approach. There are relatively few fuel consumption databases derived from field measurements, but van Leeuwen et al. (2014) provides summary statistics for African savannah burns and our low woodland savannah and grassland averages listed in Figure 11c are very close to their 0.34 kg.m^{-2} mean.

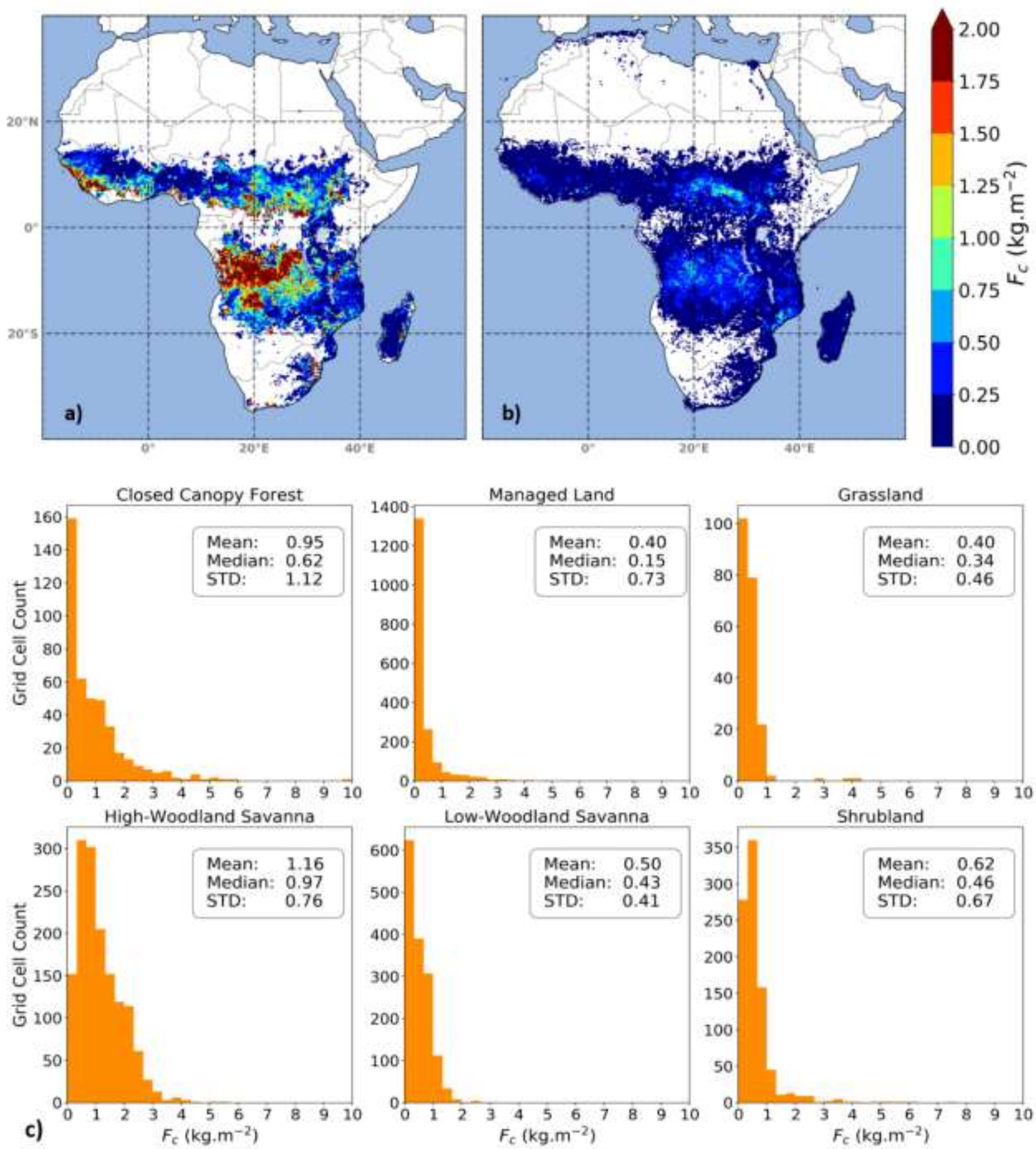

(2 columns) **Figure 11.** Fuel consumption per unit area (F_c, kg.m^{-2}) mapped at 0.25˚ from (a) 2016 FREMv2 dry matter consumed (DMC) totals and the FireCCISFD11-estimated burned area, and (b) GFEDv4.1s. (c) Per-biome FREMv2 F_c frequency distributions and derived means, medians and standard deviations. Note that F_c values in (a) apply only to the burned area patch inside a given pixel, and not the 0.25° pixel as a whole.

6. SUMMARY AND CONCLUSIONS

We have provided significant advances to the fully top-down 'Fire Radiative Energy Emissions' (FREM) landscape fire emissions methodology of Mota and Wooster (2018), and have used this to develop the highest spatio-temporal resolution African landscape fire emissions inventory currently available. The approach will form the basis of a new fire emissions product to be delivered by the EUMETSAT Land Surface Analysis Satellite Application Facility (http://landsaf.meteo.pt), and will in future be extended back to 2004 using the full Meteosat SEVIRI FRP archive already exploited to study African fires by Roberts et al. (2018b).

The FREM approach bypasses the total fuel consumption step of 'bottom up' fire emissions methodologies, recognised as a key source of uncertainty (Reid et al., 2009; Vermote et al., 2009; Van Leeuwen and Van Der Werf, 2011). The method generates smoke emissions estimates directly from satellite retrievals of FRP and relies on a set of biome-dependent smoke emission coefficients (C_{biome}, g.MJ^{-1}) that are here derived from almost one thousand matchups between Meteosat SEVIRI Fire Radiative Energy (FRE) estimates (Wooster et al., 2015) and in-plume total particulate matter (TPM) estimates made using the 1 km MAIAC AOD product (Lyapustin et al., 2018). Our FREMv2 methodology introduces significant improvements to all stages of the original FREM approach, and most particularly those associated with the prior use of the 10 km MODIS

MxD04 AOD product for TPM estimation. Issues with use of MxD04 include, masking of thick smoke as cloud (Levy et al., 2013; Raffuse et al., 2013; Remer et al., 2013; Livingston et al., 2014), the impact of sensor VZA dependence on AOD retrieval (Sayer et al., 2015; Mhawish et al., 2019), and the products' relatively low spatial resolution making plumes harder to discriminate and requiring a focus on the largest fires when deriving the FREM coefficients (Lyapustin et al., 2011; Raffuse et al., 2013; Remer et al., 2013; He et al., 2017). Our new use of the 1 km MAIAC AOD product of Lyapustin et al. (2018) addresses each of these issues, and we also derive a more up to date and detailed fire-relevant mapping of pan-African biomes using the CCI Land Cover 2015 (ESA, 2017) and Landsat-derived percentage tree cover information. The latter enables improved specification of the smoke emission coefficients in the woodland savanna biome, which annually contributes the most to Africa's fire radiative energy release. Expansion of the FREMv2 inventory to include both NHAf and SHAf enabled many more FRE-AOD matchup fires to be included in the smoke emissions coefficient generation compared to FREMv1, including many more small fires whose plumes can be discriminated using the 1 km MAIAC AODs. This also enabled localised values of plume background AOD to be selected in a more representative manner than in FREMv1 (Mota and Wooster, 2018), and the impact of relative humidity on our use of smoke mass extinction coefficient values was also assessed during our methodology.

The evolutions reported herein result in a set of FREMv2 biome-dependent smoke emission coefficients (C_{biome}) for total particulate matter 10% to 48% lower than those of FREMv1 (Mota and Wooster, 2018). The FREMv2 coefficients are now closer to those of another top-down FRP-based emissions methodology (FEER; Ichoku and Ellison 2014) compared to those of FREMv1, particularly for the low-woodland savanna, shrubland and grassland biomes which are each considerable sources of smoke emissions (Table 1). Some significant differences between the coefficients in FREMv2 and FEER do remain, but mostly in regions showing relatively few fires and thus which are rather poorly sampled by FREMv2 fire matchups. A significant advantage of FREMv2 over FEER is that the spatial mapping of the final C_e smoke emission coefficients across Africa is easily derived from the five FREMv2 C_{biome} values reported in Table 1 and the SEVIRI-pixel area biome coverage, meaning that FREMv2 C_e updates related to landcover changes can be easily calculated using only an updated landcover map. In the FEER methodology of Ichoku and Ellison (2014), C_e are mapped on a 1˚ grid cell basis from fire matchups observed within each cell using more than a decade of data from the MODIS record, and landcover change related updates thus require complete collection of a set of new fire matchups and re-derivation of C_e.

Whilst our FREMv2 approach addresses the principal uncertainties and biases in the original FREMv1 (and indeed the FEER) methodologies, there remain sources of uncertainty and limitations that will benefit from further investigation. These include:

i) Elucidation of the effect of small fires having an FRP below the minimum geostationary active fire detection limit, and the extent to which these are now accounted for via the ability to include smaller fire matchups during the C_{biome} derivation via use of the 1km MAIAC AOD product (Section 5.1)

ii) Further investigation of smoke mass extinction coefficients (β_e) used to estimated column-integrated TPM from AOD, and the relevance of smoke ageing over the period relevant here (typically < 8 hrs).

iii) Assessment of the impact of the exponential growth of the geostationary sensor pixel area far from nadir, which amplifies the non-detection of low FRP fires by raising the minimum FRP detection limit (Wooster et al., 2015).

iv) Improvement of the smoke emissions coefficients for closed canopy and managed land, which are currently derived from a relatively small number of matchup fires compared to the other biome classes.

With regards to point (iii), in the scope of any future pan-tropical and mid-latitude fire emissions product this issue can be partly overcome by applying the FREMv2 methodology to a suite of geostationary satellite FRP data, to derive a global C_e product which could then be applied to the relevant local geostationary FRP product. For example, using a GOES-derived FRP product (Xu et al., 2010) over eastern South America rather than the very high view zenith angle FRP data provided by Meteosat SEVIRI. High latitudes prove more problematic for geostationary systems, though Xu et al. (2010) did show that the high FRPs typical of crown fires in northern Canada does, to some extent, offset increased northern latitude minimum FRP detection limits, and the trade-off requires further investigation. With respect to (iii) and (iv), an increased number of fire matchups could address both, by allowing for enough samples to stratify smoke emissions coefficients by VZA as well as by biome. Including multiple years of data and focusing on improving automation of the fire match-up process, for example through use of the MAIAC QA product's 'smoke mask' (Lyapustin et al., 2012) and machine learning techniques, will help increase the range and efficiency of the matchup process and thus the number of matchups used.

We compared our FREMv2 African biomass burning emission inventory data to those of GFAS, GFED and two versions of FEER (FEER-GFASv1.2 and FEER-SEVIRI). FREMv2 provides the highest levels of spatio-temporal detail (~0.05° spatially, updated 4 times per hour) since it can exploit the native geostationary FRP data resolutions. Monthly FREMv2 TPM emission totals agreed well with both FEER-GFASv1.2 and FEER-SEVIRI, and are significantly higher than those of GFEDv4.1s and GFASv1.2 which past studies have suggested tend to underestimate NHAf and SHAf aerosol emissions (Kaiser et al., 2012; Tosca et al., 2013; Ichoku and Ellison, 2014; Reddington et al., 2016, Chevallier et al., 2009; Kopacz et al., 2010; Pechony et al., 2013). Trace gas and carbon emissions are similarly also higher than for GFEDv4.1s and GFASv1.2, but similar to those of FEER. Recent development of a 20 m African burned area (BA) product (FireCCISFD11; Roteta et al., 2019) has shown a potential reason for this, because the MODIS MCD64A1 500 m BA product, upon which GFED fire emissions estimates are based, underestimates BA by as much as 50% in some regions of Africa, and GFAS is also indirectly dependant on this BA product through its calibration against GFED (Kaiser et al., 2012).

Using the FREMv2 carbon emissions estimates we derive estimates of dry matter consumed (DMC) through an inversion of the Seiler and Crutzen (1980) approach, and dividing these by the FireCCISFD11 20 m BA product we deliver one of the first data-driven mappings of fuel consumption per unit area (F_c) across Africa, which we find produces higher F_c in many areas compared to the modelled-based GFEDv4.1s (Figure 11).

Future developments advancing the FREM approach further will include its application to FRP data from other geostationary satellites based on the same baseline algorithm applied to generate the Meteosat FRP-PIXEL product used herein (Roberts et al., 2015; Wooster et al., 2015), for example data from Himawari (Xu et al., 2017), Meteosat Indian Ocean and GOES (Xu et al., 2010). Since direct validation of large-scale fire emissions estimates remains challenging, future developments will also use the final FREMv2 smoke emissions estimates within atmospheric models to generate trace gas concentration and AOD fields for comparison to ground-based and EO-derived measures, exploiting a validation strategy similar to that previously used for evaluating other large scale fire emissions estimates (e.g. Baldassarre et al., 2015).

Acknowledgements

MODIS AOD products are distributed freely by NASA (https://search.earthdata.nasa.gov/), as is the SEVIRI FRP-PIXEL product of the EUMETSAT LAS SAF (https://landsaf.ipma.pt/). We would like to thank the LAS SAF and MODIS teams for the development and distribution of these products, as well as the developers and providers of FEER, GFAS, GFED, CCI Landcover, Landsat VCF and FireCCISFD11. We also thank Jiangping He and Tianran Zhang for their useful insights, and Mark De Jong and Thomas Dowling for their comments during editing. Funding for this work was provided by EPSRC's Centre for Doctoral Training in Cross-Disciplinary Approaches to Non-Equilibrium Systems (CANES; EP/L015854/1), NERC National Capability funding to NCEO (PR140015), NERC Grant NE/M017729/1 and by EUMETSAT's Satellite Applications Facility Programme which supports the Land Surface Analysis Satellite Application Facility (https://landsaf.ipma.pt/en/) where the Meteosat FRP-PIXEL product is generated. We also thank Alexie Lyapustin and two anonymous reviewers for their comments which have helped improve the quality and content of this article.

7. APPENDIX

Appendix A - CCI landcover classes and VCF Tree cover % assigned to each FREMv2 biome.

FREMv2 biome	Assigned CCI class codes	Landsat VCF Tree Cover above 5 m
closed canopy forest	50,180,160,170	-
low-woodland savanna	60,61,62,70,90,100,110	< 20 %
high-woodland savanna	60,61,62,70,90,100,110	> 20 %
shrubland	120,122,121	-
grassland	130,150,151,152,153	-
managed lands	10,11,12,20,30,40,190	-

Appendix B - Mean percentage contribution of different biomes to the fire radiative energy (FRE) released by fires between 2013 and 2018. On average woodland savanna fires contribute the greatest total FRE throughout the year, except for in November, and this means their determination is especially important for overall smoke emission estimate accuracy. The importance and abundance of fires in this biome is reflected in the high numbers of fire-plume matchups identified for both the *low- and high- woodland savanna* biomes (Figure 5).

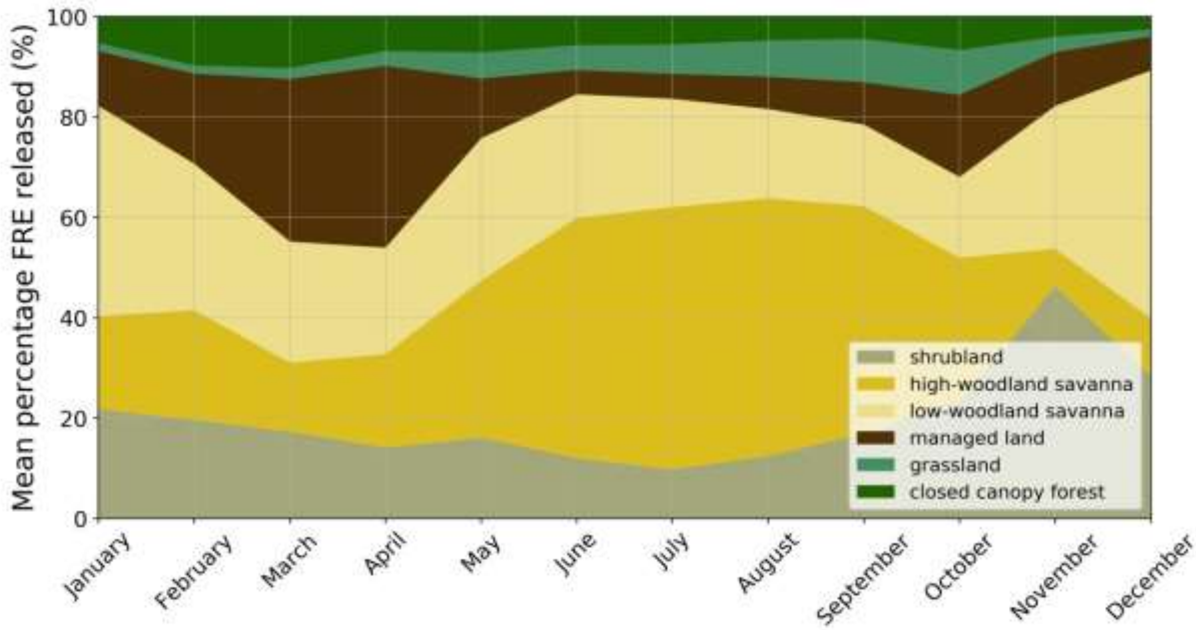

Appendix C – Percentage difference in fuel consumption per unit area (F_c, kg.m^{-2}) calculated at a 0.25˚ resolution for 2016 African fires by FREMv2 (Figure 11a) and GFEDv4.1s (Figure 11b). The former provides significantly higher values in around half of the 0.25° grid cells. Figure 11c provides the per-biome F_c statistics coming from FREMv2.

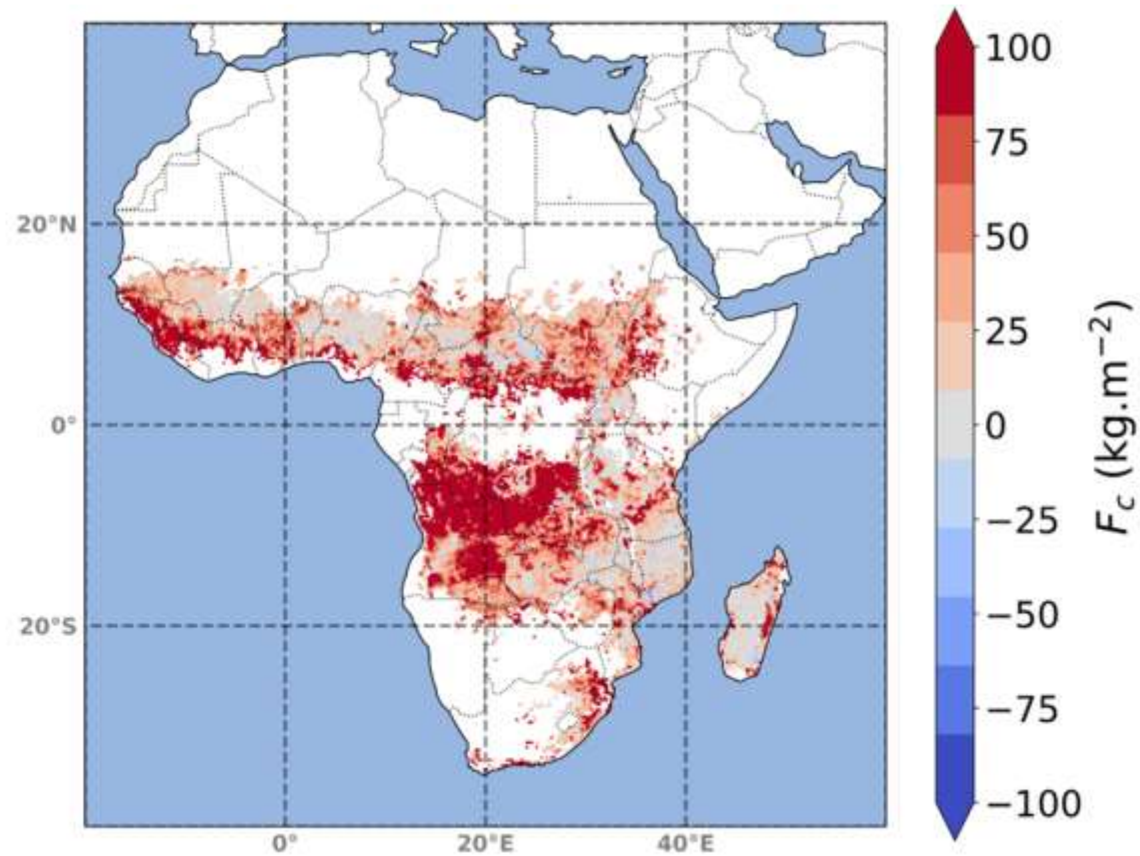

8. REFERENCES

Abel, S.J., Haywood, J.M., Highwood, E.J., Li, J., Buseck, P.R., 2003. Evolution of biomass burning aerosol properties from an agricultural fire in southern Africa. *Geophys. Res. Lett.* 30(15), pp.10–13.

Abel, S.J., Highwood, E.J., Haywood, J.M., Stringer, M.A., 2005. The direct radiative effect of biomass burning aerosols over southern Africa. *Atmos. Chem. Phys. Discuss.* 5(2), pp.1165–1211.

Akagi, S.K., Yokelson, R.J., Wiedinmyer, C., Alvarado, M.J., Reid, J.S., Karl, T., Crounse, J.D., Wennberg, P.O., 2011. Emission factors for open and domestic biomass burning for use in atmospheric models. *Atmos. Chem. Phys.* 11(9), pp.4039–4072.

Andela, N., Kaiser, J.W., Van Der Werf, G.R., Wooster, M.J., 2015. New fire diurnal cycle characterizations to improve fire radiative energy assessments made from MODIS observations. *Atmos. Chem. Phys.* 15, pp.8831–8846.

Andreae, M.O., 2019. Emission of trace gases and aerosols from biomass burning - An updated assessment. *Atmos. Chem. Phys.* 19(13), pp.8523–8546.

Andreae, M.O., Merlet, P., 2001. Emissions of trace gases and aerosols from biomass burning. *Global Biogeochem. Cycles* 15(4), pp.955–966.

Arvani, B., Pierce, R.B., Lyapustin, A., Wang, Y., Ghermandi, G., Teggi, S., 2016. Seasonal monitoring and estimation of regional aerosol distribution over Po valley, northern Italy, using a high-resolution MAIAC product. *Atmos. Environ.* 141, pp.106–121.

Baldassarre, G., Pozzoli, L., Schmidt, C.C., Unal, A., Kindap, T., Menzel, W.P., Whitburn, S., Coheur, P.-F., Kavgaci, A., Kaiser, J.W., 2015. Using SEVIRI fire observations to drive smoke plumes in the CMAQ air quality model: the case of Antalya in 2008. *Atmos. Chem. Phys.* 15, pp.8539–8558.

Balsamo, G., Albergel, C., Beljaars, A., Boussetta, S., Brun, E., Cloke, H., Dee, D., Dutra, E., 2015. ERA-Interim / Land : a global land surface reanalysis data set pp.389–407.

Boschetti, L., Eva, H.D., Brivio, P.A., Grégoire, J.M., 2004. Lessons to be learned from the comparison of three satellite-derived biomass burning products. *Geophys. Res. Lett.* 31(21), pp.2–5.

Chevallier, F., Fortems, A., Bousquet, P., Pison, I., Szopa, S., Devaux, M., Hauglustaine, D.A., 2009. African CO emissions between years 2000 and 2006 as estimated from MOPITT observations. *Biogeosciences* 6(1), pp.103–111.

Chin, M., Ginoux, P., Kinne, S., Torres, O., Holben, B., Duncan, B.N., Martin, R. V, Logan, J. a., Higurashi, A., Nakajima, T., 2002. Tropospheric Aerosol Optical Thickness from the GOCART Model and Comparisons with Satellite and Sun Photometer Measurements. *J. Atmos. Sci.* 59(3), pp.461–483.

Chu, D.A., Kaufman, Y., Ichoku, C., Remer, L.A., Tanre, D., Holben, B., 2002. Validation of MODIS aerosol optical depth retrieval over land 29(12), pp.4–7.

Crutzen, P.J., Andreae, M.O., 1990. Biomass Burning in the Tropics: Impact on Atmospheric Chemistry and Biogeochemical Cycles. *Science (80-.).* 250(4988), pp.1669–1678.

Darmenov, A.S., da Silva, A., 2015. The Quick Fire Emissions Dataset (QFED) - Documentation of versions 2.1, 2.2 and 2.4. *NASA Tech. Rep. Ser. Glob. Model. Data Assim.* 38(September).

Ellicott, E., Vermote, E., Giglio, L., Roberts, G., 2009. Estimating biomass consumed from fire using MODIS FRE. *Geophys. Res. Lett.* 36(13).

Emili, E., Lyapustin, A., Wang, Y., Popp, C., Korkin, S., Zebisch, M., Wunderle, S., Petitta, M., 2011. High spatial resolution aerosol retrieval with MAIAC: Application to mountain regions. *J. Geophys. Res. Atmos.* 116(23), pp.1–12.

ESA, 2017. European Space Agency Landcover CCI Product User Guide Version 2.0.

Flannigan, M.D., Vonder Haar, T.H., 1986. Forest fire monitoring using NOAA satellite AVHRR. *Can. J. For. Researrch* 16(5), pp.975–982.

Formenti, P., Elbert, W., Maenhaut, W., Haywood, J.M., Osborne, S., Andreae, M.O., 2003. Inorganic and carbonaceous aerosols during the Southern African Regional Science Initiative (SAFARI 2000) experiment: Chemical characteristics, physical properties, and emission data or smoke from African biomass burning. *J. Geophys. Res. D Atmos.* 108(13), pp.1–16.

Forster, P., Ramaswamy, V., Artaxo, P., Berntsen, T., Betts, R., Fahey, D.W., Haywood, J.M., Lean, J., Lowe, D.C., Myhre, G., Nganga, J., Prinn, R., Raga, G., Schulz, M., Van Dorland, R., 2007. Changes in Atmospheric Constituents and in Radiative Forcing (IPCC 2007). *Change* 30(22), pp.129–234.

Freeborn, P.H., Wooster, M.J., Hao, W.M., Ryan, C.A., Nordgren, B.L., Baker, S.P., Ichoku, C., 2008. Relationships between energy release , fuel mass loss , and trace gas and aerosol emissions during laboratory biomass fires 113, pp.1–17.

Freeborn, P.H., Wooster, M.J., Roberts, G., 2011. Addressing the spatiotemporal sampling design of MODIS to provide estimates of the fire radiative energy emitted from Africa. *Remote Sens. Environ.* 115(2), pp.475–489.

Freeborn, P.H., Wooster, M.J., Roberts, G., Malamud, B.D., Xu, W., 2009. Development of a virtual active fire product for Africa through a synthesis of geostationary and polar orbiting satellite data. *Remote Sens. Environ.* 113(8), pp.1700–1711.

Giglio, L., 2007. Characterization of the tropical diurnal fire cycle using VIRS and MODIS observations. *Remote Sens. Environ.* 108(4), pp.407–421.

Giglio, L., Boschetti, L., Roy, D., Humber, M.L., Justice, C.O., 2018. The Collection 6 MODIS burned area mapping algorithm and product. *Remote Sens. Environ.* 217(August), pp.72–85.

Giglio, L., Descloitres, J., Justice, C.O., Kaufman, Y., 2003. An enhanced contextual fire detection algorithm for MODIS. *Remote Sens. Environ.* 87(2–3), pp.273–282.

Giglio, L., Loboda, T., Roy, D., Quayle, B., Justice, C.O., 2009. An active-fire based burned area mapping algorithm for the MODIS sensor. *Remote Sens. Environ.* 113(2), pp.408–420.

Giglio, L., Randerson, J.T., Van Der Werf, G.R., 2013. Analysis of daily, monthly, and annual burned area using the fourth-generation global fire emissions database (GFED4). *J. Geophys. Res. Biogeosciences* 118(1), pp.317–328.

Giglio, L., Schroeder, W., Justice, C.O., 2016. The collection 6 MODIS active fire detection algorithm and fire products. *Remote Sens. Environ.* 178, pp.31–41.

Giglio, L., Van Der Werf, G.R., Randerson, J.T., Collatz, G.J., Kasibhatla, P.S., 2006. Global estimation of burned area using MODIS active fire observations. *Atmos. Chem. Phys.* 6(4), pp.957–974.

Hall, J.V., Zhang, R., Schroeder, W., Huang, C., Giglio, L., 2019. Validation of GOES-16 ABI and MSG SEVIRI active fire products. *Int. J. Appl. Earth Obs. Geoinf.* 83(August), pp.101928.

Hansen, M.C., DeFries, R.S., Townshend, J.R.G., Sohlberg, R., Dimiceli, C., Carroll, M., 2002. Towards an operational MODIS continuous field of percent tree cover algorithm: Examples using AVHRR and MODIS data. *Remote Sens. Environ.* 83(1–2), pp.303–319.

Hawbaker, T.J., Vanderhoof, M.K., Beal, Y.J., Takacs, J.D., Schmidt, G.L., Falgout, J.T., Williams, B., Fairaux, N.M., Caldwell, M.K., Picotte, J.J., Howard, S.M., Stitt, S., Dwyer, J.L., 2017. Mapping burned areas using dense time-series of Landsat data. *Remote Sens. Environ.* 198(September), pp.504–522.

He, Q., Zhang, M., Huang, B., Tong, X., 2017. MODIS 3 km and 10 km aerosol optical depth for China: Evaluation and comparison. *Atmos. Environ.* 153, pp.150–162.

Heil, A., Kaiser, J.W., Van Der Werf, G.R., Wooster, M.J., Schultz, M.G., van der Gon, H.D., 2010. Assessment of the Real-Time Fire Emissions (GFASv0) by MACC. *ECMWF Tech. Memo.* 628(July), pp.1–47.

Holben, B., Tanre, D., Smirnov, A., Eck, T.F., Slutsker, I., Abuhassan, N., Newcomb, W.W., Schafer, J.S., Chatenet, B., Lavenu, F., Kaufman, Y., Castle, J.V., Setzer, A., Markham, B., Clark, D., Frouin, R., Halthore, R., Karneli, A., O'Neill, N.T., 2001. An Emerging Ground-based Aerosol Climatology: Aerosol Optical Depth from AERONET. *J. Geophys. Res.* 106(Dll), pp.12067–12097.

Hsu, N.C., Jeong, M., Bettenhausen, C., Sayer, A.M., Hansell, R., Seftor, C.S., Huang, J., Tsay, S.C., 2013. Enhanced Deep Blue aerosol retrieval algorithm: The second generation. *J. Geophys. Res. Atmos.* 118(16), pp.9296–9315.

Hsu, N.C., Tsay, S.C., King, M.D., Herman, J.R., 2006. Deep Blue retrievals of Asian aerosol properties during ACE-Asia. *IEEE Trans. Geosci. Remote Sens.* 44(11), pp.3180–3195.

Hsu, N.C., Tsay, S.C., King, M.D., Kaufman, Y., Herman, J.R., Goddard, N., Flight, S., 2004.

Aerosol Properties over “ Bright-Reflecting. *IEEE Trans. Geosci. Remote Sens.* 42(3), pp.23.

Hu, X., Waller, L.A., Lyapustin, A., Wang, Y., Al-Hamdan, M.Z., Crosson, W.L., Estes, M.G., Estes, S.M., Quattrochi, D.A., Puttaswamy, S.J., Liu, Y., 2014. Estimating ground-level PM2.5 concentrations in the Southeastern United States using MAIAC AOD retrievals and a two-stage model. *Remote Sens. Environ.* 140, pp.220–232.

Huijnen, V., Wooster, M.J., Kaiser, J.W., Gaveau, D.L.A., Flemming, J., Parrington, M., Inness, A., Murdiyarso, D., Main, B., Van Weele, M., 2016. Fire carbon emissions over maritime southeast Asia in 2015 largest since 1997. *Sci. Rep.* 6(May), pp.1–8.

Ichoku, C., Chu, D.A., Mattoo, S., Kaufman, Y., Remer, L.A., Tanre, D., Slutsker, I., Holben, B., 2002. A spatio-temporal approach for global validation and analysis of MODIS aerosol products 29(12), pp.1–4.

Ichoku, C., Ellison, L., 2014. Global top-down smoke-aerosol emissions estimation using satellite fire radiative power measurements. *Atmos. Chem. Phys.* 14(13), pp.6643–6667.

Ichoku, C., Kaufman, Y., 2005. A method to derive smoke emission rates from MODIS fire radiative energy measurements. *IEEE Trans. Geosci. Remote Sens.* 43(11), pp.2636–2649.

Ichoku, C., Martins, J.V., Kaufman, Y., Wooster, M.J., Freeborn, P.H., Hao, W.M., Baker, S.P., Ryan, C.A., Nordgren, B.L., 2008. Laboratory investigation of fire radiative energy and smoke aerosol emissions 113, pp.1–11.

Ichoku, C., Remer, L.A., Kaufman, Y., Levy, R., Chu, D.A., Tanre, D., Holben, B., 2003. MODIS observation of aerosols and estimation of aerosol radiative forcing over southern Africa during SAFARI 2000. *J. Geophys. Res. Atmos.* 108(D13), pp.n/a-n/a.

Jethva, H., Torres, O., Yoshida, Y., 2019. Accuracy assessment of MODIS land aerosol optical thickness algorithms using AERONET measurements over North America. *Atmos. Meas. Tech.*

Justice, C.O., Giglio, L., Korontzi, S., Owens, J., Morisette, J.T., Roy, D., Descloitres, J., Alleaume, S., Petitcolin, F., Kaufman, Y., 2002. The MODIS fire products. *Remote Sens. Environ.* 83(1–2), pp.244–262.

Kaiser, J.W., Heil, A., Andreae, M.O., Benedetti, A., Chubarova, N., Jones, L., Morcrette, J.J., Razinger, M., Schultz, M.G., Suttie, M., Van Der Werf, G.R., 2012. Biomass burning emissions estimated with a global fire assimilation system based on observed fire radiative power. *Biogeosciences* 9(1), pp.527–554.

Kasischke, E.S., Penner, J.E., 2004. Improving global estimates of atmospheric emissions from biomass burning. *J. Geophys. Res. D Atmos.* 109(14), pp.1–9.

Knorr, W., Lehsten, V., Arneth, A., 2012. Determinants and predictability of global wildfire emissions. *Atmos. Chem. Phys.* 12(15), pp.6845–6861.

Kobayashi, T., Tsend-Ayush, J., Tateishi, R., 2016. A new global tree-cover percentage map using MODIS data. *Int. J. Remote Sens.* 37(4), pp.969–992.

Kopacz, M., Jacob, D.J., Fisher, J.A., Logan, J.A., Zhang, L., Megretskaia, I.A., Yantosca, R.M., Singh, K., Henze, D.K., Burrows, J.P., Buchwitz, M., Khlystova, I., McMillan, W.W., Gille, J.C., Edwards, D.P., Eldering, A., Thouret, V., Nedelec, P., 2010. Global estimates of CO sources with high resolution by adjoint inversion of multiple satellite datasets (MOPITT, AIRS, SCIAMACHY, TES). *Atmos. Chem. Phys.* 10(3), pp.855–876.

Koppmann, R., von Czapiewski, K., Reid, J.S., 2005. A review of biomass burning emissions, part 1: gaseous emissions of carbon monoxide, methane, volatile organic compounds, and nitrogen containing compounds. *Atmos. Chem. Phys. Discuss.* (5), pp.10455–10516.

Korontzi, S., Roy, D., Justice, C.O., Ward, D.E., 2004. Modeling and sensitivity analysis of fire emissions in southern Africa during SAFARI 2000. *Remote Sens. Environ.* 92(2), pp.255–275.

Larkin, N.K., Raffuse, S.M., Strand, T.M., 2014. Wildland fire emissions, carbon, and climate: U.S. emissions inventories. *For. Ecol. Manage.* 317, pp.61–69.

Lavrov, A., Utkin, A.B., Vilar, R., Fernandes, A., 2006. Evaluation of smoke dispersion from forest fire plumes using lidar experiments and modelling. *Int. J. Therm. Sci.* 45(9), pp.848–859.

Lehsten, V., Tansey, K., Balzter, H., Thonicke, K., Spessa, A., Weber, U., Smith, B., Arneth, A., 2009. Estimating carbon emissions from African wildfires. *Biogeosciences* 6, pp.349–360.

Levy, R., Mattoo, S., Munchak, L.A., Remer, L.A., Sayer, A.M., Patadia, F., Hsu, N.C., 2013. The Collection 6 MODIS aerosol products over land and ocean. *Atmos. Meas. Tech.* 6(11), pp.2989–3034.

Lindeberg, T., 1998. Feature Detection with Automatic Scale Selection. *Int. J. Comput. Vis.* 16(2), pp.79–116.

Livingston, J.M., Redemann, J., Shinozuka, Y., Johnson, R., Russell, P.B., Zhang, Q., Mattoo, S., Remer, L.A., Levy, R., Munchak, L.A., Ramachandran, S., 2014. Comparison of MODIS 3 km and 10 km resolution aerosol optical depth retrievals over land with airborne sunphotometer measurements during ARCTAS summer 2008. *Atmos. Chem. Phys.* 14(4), pp.2015–2038.

Lu, X., Zhang, X., Li, F., Cochrane, M.A., 2019. Investigating Smoke Aerosol Emission Coefficients using MODIS Active Fire and Aerosol Products — A Case Study in the

CONUS and Indonesia. *J. Geophys. Res. Biogeosciences* pp.1–17.

Lyapustin, A., Korkin, S., Wang, Y., Quayle, B., Laszlo, I., 2012. Discrimination of biomass burning smoke and clouds in MAIAC algorithm. *Atmos. Chem. Phys.* 12(20), pp.9679–9686.

Lyapustin, A., Wang, Y., Korkin, S., Huang, D., 2018. MODIS Collection 6 MAIAC algorithm. *Atmos. Meas. Tech.* 11(10), pp.5741–5765.

Lyapustin, A., Wang, Y., Laszlo, I., Kahn, R.A., Korkin, S., Remer, L.A., Levy, R., Reid, J.S., 2011. Multiangle implementation of atmospheric correction (MAIAC): 2. Aerosol algorithm. *J. Geophys. Res. Atmos.* 116(3), pp.1–15.

Martins, V.S., Barbosa, C.C.F., De Carvalho, L.A.S., Jorge, D.S.F., Lobo, F. de L., de Moraes Novo, E.M.L., 2017. Assessment of atmospheric correction methods for sentinel-2 MSI images applied to Amazon floodplain lakes. *Remote Sens.* 9(4).

Mhawish, A., Banerjee, T., Sorek-Hamer, M., Lyapustin, A., Broday, D.M., Chatfield, R., 2019. Comparison and evaluation of MODIS Multi-angle Implementation of Atmospheric Correction (MAIAC) aerosol product over South Asia. *Remote Sens. Environ.* 224(February 2018), pp.12–28.

Mota, B., Wooster, M.J., 2018. A new top-down approach for directly estimating biomass burning emissions and fuel consumption rates and totals from geostationary satellite fi re radiative power (FRP). *Remote Sens. Environ.* 206(February 2017), pp.45–62.

Pechony, O., Shindell, D.T., Faluvegi, G., 2013. Direct top-down estimates of biomass burning CO emissions using TES and MOPITT versus bottom-up GFED inventory. *J. Geophys. Res. Atmos.* 118(14), pp.8054–8066.

Pereira, J.M.C., Pereira, B.S., Barbosa, P.M., Stroppiana, D., Vasconcelos, M.J.P., Gregoire, J.M., 1999. Satellite monitoring of fire in the EXPRESSO study area during the 1996 dry season experiment: Active fires, burnt area, and atmospheric emissions. *J. Geophys. Res.* 104(D23), pp.30701–30712.

Quennehen, B., Schwarzenboeck, A., Matsuki, A., Burkhart, J.F., Stohl, A., Ancellet, G., Law, K.S., 2012. Anthropogenic and forest fire pollution aerosol transported to the Arctic: Observations from the POLARCAT-France spring campaign. *Atmos. Chem. Phys.* 12(14), pp.6437–6454.

Raffuse, S.M., McCarthy, M.C., Craig, K.J., Dewinter, J.L., Jumbam, L.K., Fruin, S., James Gauderman, W., Lurmann, F.W., 2013. High-resolution MODIS aerosol retrieval during wildfire events in California for use in exposure assessment. *J. Geophys. Res. Atmos.* 118(19), pp.11242–11255.

Randerson, J.T., Chen, Y., Van Der Werf, G.R., Rogers, B.M., Morton, D.C., 2012. Global burned area and biomass burning emissions from small fires. *J. Geophys. Res. G Biogeosciences* 117(4).

Randerson, J.T., Liu, H., Flanner, M.G., Chambers, S.D., Jin, Y., Hess, P.G., Pfister, G., Mack, M.C., Treseder, K.K., Welp, L.R., Chapin, F.S., Harden, J.W., Goulden, M.L., Lyons, E., Neff, J.C., Schuur, E.A.G., Zender, C.S., 2006. The impact of boreal forest fire on climate warming. *Science (80-.).* 314(5802), pp.1130–1132.

Reddington, C.L., Spracklen, D. V., Artaxo, P., Ridley, D.A., Rizzo, L. V., Arana, A., 2016. Analysis of particulate emissions from tropical biomass burning using a global aerosol model and long-term surface observations. *Atmos. Chem. Phys.* 16(17), pp.11083–11106.

Reid, J.S., Hobbs, P. V., Ferek, R.J., Blake, D.R., Martins, J.V., Dunlap, M.R., Liousse, C., 1998. Physical, chemical, and optical properties of regional hazes dominated by smoke in

Brazil. *J. Geophys. Res. Atmos.* 103(D24), pp.32059–32080.

Reid, J.S., Hyer, E.J., Prins, E., Westphal, D.L., Zhang, J., Wang, J., Christopher, S.A., Curtis, C.A., Schmidt, C.C., Eleuterio, D.P., Richardson, K.A., Hoffman, J.P., 2009. Global monitoring and forecasting of biomass-burning smoke: Description of and lessons from the fire Locating and Modeling of Burning Emissions (FLAMBE) program. *IEEE J. Sel. Top. Appl. Earth Obs. Remote Sens.* 2(3), pp.144–162.

Reid, J.S., Koppmann, R., Eck, T.F., Eleuterio, D.P., 2005. A review of biomass burning emissions part II : intensive physical properties of biomass burning particles. *Atmos. Chem. Phys.* 4(5), pp.799–825.

Remer, L.A., Kaufman, Y., Tanre, D., Mattoo, S., Chu, D.A., Martins, J.V., Li, R.-R., Ichoku, C., Levy, R., Kleidman, R., Eck, T.F., Vermote, E., 2005. The MODIS Aerosol Algorithm, Products, and Validation. *J. Atmos. Sci.* 62(4), pp.947–973.

Remer, L.A., Mattoo, S., Levy, R., Munchak, L.A., 2013. MODIS 3 km aerosol product: Algorithm and global perspective. *Atmos. Meas. Tech.* 6(7), pp.1829–1844.

Roberts, G., Wooster, M.J., 2008. Fire detection and fire characterization over Africa using meteosat SEVIRI. *IEEE Trans. Geosci. Remote Sens.* 46(4), pp.1200–1218.

Roberts, G., Wooster, M.J., Freeborn, P.H., Xu, W., 2011. Integration of geostationary FRP and polar-orbiter burned area datasets for an enhanced biomass burning inventory. *Remote Sens. Environ.* 115(8), pp.2047–2061.

Roberts, G., Wooster, M.J., Lauret, N., Gastellu-Etchegorry, J.P., Lynham, T., McRae, D., 2018a. Investigating the impact of overlying vegetation canopy structures on fire radiative power (FRP) retrieval through simulation and measurement. *Remote Sens. Environ.* 217(March), pp.158–171.

Roberts, G., Wooster, M.J., Perry, G.L.W., Drake, N., Rebelo, L.M., Dipotso, F., 2005. Retrieval of biomass combustion rates and totals from fire radiative power observations: Application to southern Africa using geostationary SEVIRI imagery. *J. Geophys. Res. Atmos.* 110(21), pp.1–19.

Roberts, G., Wooster, M.J., Xu, W., Freeborn, P.H., Morcrette, J.J., Jones, L., Benedetti, A., Jiangping, H., Fisher, D., Kaiser, J.W., 2015. LSA SAF Meteosat FRP products-Part 2: Evaluation and demonstration for use in the Copernicus Atmosphere Monitoring Service (CAMS). *Atmos. Chem. Phys.* 15(22), pp.13241–13267.

Roberts, G., Wooster, M.J., Xu, W., He, J., 2018b. Fire activity and fuel consumption dynamics in sub-Saharan Africa. *Remote Sens.* 10(10), pp.1–22.

Roteta, E., Bastarrika, A., Padilla, M., Storm, T., Chuvieco, E., 2019. Development of a Sentinel-2 burned area algorithm: Generation of a small fire database for sub-Saharan Africa. *Remote Sens. Environ.* 222(September 2017), pp.1–17.

Sayer, A.M., Hsu, N.C., Bettenhausen, C., 2015. Implications of MODIS bowtie distortion on aerosol optical depth retrievals , and techniques for mitigation pp.8727–8752.

Sayer, A.M., Hsu, N.C., Bettenhausen, C., Jeong, M., 2013. Validation and uncertainty estimates for MODIS Collection 6 “deep Blue” aerosol data. *J. Geophys. Res. Atmos.* 118(14), pp.7864–7872.

Sayer, A.M., Munchak, L.A., Hsu, N.C., Levy, R., Bettenhausen, C., Jeong, M., 2014. MODIS Collection 6 aerosol products : Comparison between Aqua ’ s e-Deep Blue , Dark Target , and “ merged ” data sets ,.

Schroeder, W., Oliva, P., Giglio, L., Csiszar, I., 2014. The New VIIRS 375m active fire detection data product: Algorithm description and initial assessment. *Remote Sens. Environ.* 143, pp.85–96.

Schultz, M.G., Heil, A., Hoelzemann, J.J., Spessa, A., Thonicke, K., Goldammer, J.G., Held, A.C., Pereira, J.M.C., van Het Bolscher, M., 2008. Global wildland fire emissions from 1960 to 2000. *Global Biogeochem. Cycles* 22(2), pp.1–17.

Seiler, W., Crutzen, P.J., 1980. Estimates of gross and net fluxes of carbon between the biosphere and the atmosphere from biomass burning. *Clim. Change* 2(3), pp.207–247.

Sexton, J.O., Song, X.P., Feng, M., Noojipady, P., Anand, A., Huang, C., Kim, D.H., Collins, K.M., Channan, S., DiMiceli, C., Townshend, J.R.G., 2013. Global, 30-m resolution continuous fields of tree cover: Landsat-based rescaling of MODIS vegetation continuous fields with lidar-based estimates of error. *Int. J. Digit. Earth* 6(5), pp.427–448.

Superczynski, S., Kondragunta, S., Lyapustin, A., 2017. Evaluation of the multi-angle implementation of atmospheric correction (MAIAC) aerosol algorithm through intercomparison with VIIRS aerosol products and AERONET. *J. Geophys. Res.* 122(5), pp.3005–3022.

Tanre, D., Kaufman, Y., Herman, M., Mattoo, S., 1997. Remote sensing of aerosol properties over oceans using the MODIS/EOS spectral radiances. *J. Geophys. Res. Atmos.* 102(D14), pp.16971–16988.

Tsela, P., Wessels, K., Botai, J., Archibald, S., Swanepoel, D., Steenkamp, K., Frost, P., 2014. Validation of the two standard MODIS satellite burned-area products and an empirically-derived merged product in South Africa. *Remote Sens.* 6(2), pp.1275–1293.

Van Der Werf, G.R., Randerson, J.T., Giglio, L., Collatz, G.J., Kasibhatla, P.S., Arellano, A. F., J., 2006. Interannual variability in global biomass burning emissions from 1997 to 2004. *Atmos. Chem. Phys.* 6(11), pp.3423–3441.

Van Der Werf, G.R., Randerson, J.T., Giglio, L., Collatz, G.J., Mu, M., Kasibhatla, P.S., Morton, D.C., Defries, R.S., Jin, Y., Van Leeuwen, T.T., 2010. Global fire emissions and the contribution of deforestation, savanna, forest, agricultural, and peat fires (1997-2009). *Atmos. Chem. Phys.* 10(23), pp.11707–11735.

Van Der Werf, G.R., Randerson, J.T., Giglio, L., Van Leeuwen, T.T., Chen, Y., Rogers, B.M., Mu, M., van Marle, M.J.E., Morton, D.C., Collatz, G.J., Yokelson, R.J., Kasibhatla, P.S., 2017. Global fire emissions estimates during 1997-2015. *Earth Syst. Sci. Data Discuss.* pp.1–43.

Van Leeuwen, T.T., Van Der Werf, G.R., 2011. Spatial and temporal variability in the ratio of trace gases emitted from biomass burning. *Atmos. Chem. Phys.* 11(8), pp.3611–3629.

van Leeuwen, T.T., van der Werf, G.R., Hoffmann, A.A., Detmers, R.G., Rücker, G., French, N.H.F., Archibald, S., Carvalho, J.A., Cook, G.D., de Groot, W.J., Hély, C., Kasischke, E.S., Kloster, S., McCarty, J.L., Pettinari, M.L., Savadogo, P., Alvarado, E.C., Boschetti, L., Manuri, S., Meyer, C.P., Siegert, F., Trollope, L.A., Trollope, W.S.W., 2014. Biomass burning fuel consumption rates: a field measurement database. *Biogeosciences Discuss.* 11(6), pp.8115–8180.

Van Leeuwen, T.T., Van Der Werf, G.R., Hoffmann, A.A., Detmers, R.G., Rücker, G., French, N.H.F., Archibald, S., Carvalho, J.A., Cook, G.D., De Groot, W.J., Hély, C., Kasischke, E.S., Kloster, S., McCarty, J.L., Pettinari, M.L., Savadogo, P., Alvarado, E.C., Boschetti, L., Manuri, S., Meyer, C.P., Siegert, F., Trollope, L.A., Trollope, W.S.W., 2014. Biomass burning fuel consumption rates: A field measurement database. *Biogeosciences* 11(24), pp.7305–7329.

Van Wilgen, B.W., Higgins, K.B., Bellstedt, D.U., 1990. The role of vegetation structure and fuel chemistry in excluding fire from forest patches in the fire-prone fynbos shrublands of South

Africa. *J. Ecol.*

Veefkind, J.P., Aben, I., McMullan, K., Förster, H., de Vries, J., Otter, G., Claas, J., Eskes, H.J., de Haan, J.F., Kleipool, Q., van Weele, M., Hasekamp, O., Hoogeveen, R., Landgraf, J., Snel, R., Tol, P., Ingmann, P., Voors, R., Kruizinga, B., Vink, R., Visser, H., Levelt, P.F., 2012. TROPOMI on the ESA Sentinel-5 Precursor: A GMES mission for global observations of the atmospheric composition for climate, air quality and ozone layer applications. *Remote Sens. Environ.* 120(2012), pp.70–83.

Vermote, E., Ellicott, E., Dubovik, O., Lapyonok, T., Chin, M., Giglio, L., Roberts, G., 2009. An approach to estimate global biomass burning emissions of organic and black carbon from MODIS fire radiative power. *J. Geophys. Res. Atmos.* 114(18), pp.1–22.

Westerling, A.L., Hidalgo, H.G., Cayan, D.R., Swetnam, T.W., 2006. Warming and earlier spring increase Western U.S. forest wildfire activity. *Science (80-.).* 313, pp.940–843.

Wiedinmyer, C., Akagi, S.K., Yokelson, R.J., Emmons, L.K., Al-Saadi, J.A., Orlando, J.J., Soja, A.J., 2011. The Fire INventory from NCAR (FINN): A high resolution global model to estimate the emissions from open burning. *Geosci. Model Dev.* 4(3), pp.625–641.

Wolfe, R.E., Roy, D., Vermote, E., 1998. MODIS Land Data Storage , Gridding , and Compositing Methodology : Level 2 Grid 36(4), pp.1324–1338.

Wooster, M.J., Freeborn, P.H., Archibald, S., Oppenheimer, C., Roberts, G., Smith, T.E.L., Govender, N., Burton, M., Palumbo, I., 2011. Field determination of biomass burning emission ratios and factors via open-path FTIR spectroscopy and fire radiative power assessment: Headfire, backfire and residual smouldering combustion in African savannahs. *Atmos. Chem. Phys.* 11(22), pp.11591–11615.

Wooster, M.J., Roberts, G., Freeborn, P.H., Xu, W., Govaerts, Y., Beeby, R., He, J., Lattanzio, A., Fisher, D., Mullen, R., 2015. LSA SAF Meteosat FRP products-Part 1: Algorithms, product contents, and analysis. *Atmos. Chem. Phys.* 15(22), pp.13217–13239.

Wooster, M.J., Roberts, G., Perry, G.L.W., Kaufman, Y., 2005. Retrieval of biomass combustion rates and totals from fire radiative power observations: FRP derivation and calibration relationships between biomass consumption and fire radiative energy release. *J. Geophys. Res. Atmos.* 110(24), pp.1–24.

Worden, H.M., Deeter, M.N., Edwards, D.P., Gille, J.C., Drummond, J.R., Nédélec, P., 2010. Observations of near-surface carbon monoxide from space using MOPITT multispectral retrievals. *J. Geophys. Res. Atmos.* 115(18), pp.1–12.

Xiao, Q., Zhang, H., Choi, M., Li, S., Kondragunta, S., Kim, J., Holben, B., Levy, R., Liu, Y., 2016. Evaluation of VIIRS, GOCI, and MODIS Collection 6 AOD retrievals against ground sunphotometer observations over East Asia. *Atmos. Chem. Phys.* 16(3), pp.1255–1269.

Xu, W., Wooster, M.J., Kaneko, T., He, J., Zhang, T., Fisher, D., 2017. Major advances in geostationary fire radiative power (FRP) retrieval over Asia and Australia stemming from use of Himarawi-8 AHI. *Remote Sens. Environ.* 193, pp.138–149.

Xu, W., Wooster, M.J., Roberts, G., Freeborn, P.H., 2010. Remote Sensing of Environment New GOES imager algorithms for cloud and active fi re detection and fi re radiative power assessment across North , South and Central America. *Remote Sens. Environ.* 114(9), pp.1876–1895.

Yevich, R., Logan, J.A., 2003. An assessment of biofuel use and burning of agricultural waste in the developing world. *Global Biogeochem. Cycles* 17(4), pp.n/a-n/a.

Zhang, T., 2018. How Well Does the ‘ Small Fire Boost ’ Methodology Used within the GFED4 . 1s Fire Emissions Database Represent the Timing , Location and Magnitude of Agricultural

Burning ?

Zhang, T., Wooster, M.J., Xu, W., 2017. Approaches for synergistically exploiting VIIRS I- and M-Band data in regional active fire detection and FRP assessment: A demonstration with respect to agricultural residue burning in Eastern China. *Remote Sens. Environ.* 198, pp.407–424.

Zhou, L., Wang, Y., Chi, Y., Wang, S., Wang, Q., 2019. Contrasting post-fire dynamics between Africa and South America based on MODIS observations. *Remote Sens.* 11(9).

9. LIST OF FIGURE CAPTIONS

Figure 1.

Example plume from a fire burning north of the Save River (Mozambique), imaged on the morning of 8th October 2015 at 11:15 UTC via the Aqua satellites MODIS sensor (at a VZA 40.6°). (a) 10 km MxD04_DB AOD product; (b) MxD04_DB field showing the number of 1 km reflectance pixels (out of 100) used to retrieve each 10 km AOD pixel value; (c) 500 m MODIS Corrected Reflectance (True Colour) image; and (d) 1 km MCD19 MAIAC AOD product derived from the same MODIS imagery shown in (c). The colour scale shown in (d) is also relevant for (a). The plume is far more easily distinguished in the 1 km than the 10 km AOD product and better matched to the smoke spatial distribution shown in the MODIS true colour image of (c). Unlike the 1 km AOD product of (d), the 10 km MxD04_BD AOD data of (a) rather poorly defines the plume bounds and some pixels in this product are heavily impacted by the cloud mask which removes AOD pixels over the thickest smoke (b). Some erroneous masking does occur in the 1 km product of (d), shown as the black pixels, but this is minimal and addressed via the interpolation described in Section 4.3.

Figure 2.

(a) Estimated fire emitted Total Particulate Matter (TPM) in 635 individual smoke plumes, as derived from the 10 km MxD04_DB AOD product (*orange*) and the 1 km MAIAC AOD product (*blue*), shown as a function of sensor view zenith angle (VZA). (b) Direct comparison of the matching MxD04_DB and MAIAC-derived TPM values for each plume, restricted to plumes observed at VZA ≤ 20˚. TPM is calculated from AOD using the equations presented in Ichoku and Kaufman (2005) as described in Section 4.4.

Figure 3.

(a) Mapped percentage tree cover above 5 metres, as determined from the 30 m spatial resolution Landsat Vegetation Continuous fields (VCF) product for 2015. (b) FREMv2 biome map for Africa derived from the 2015 ESA CCI Landcover map (itself derived from 300 m PROBA-V imagery) and the Landsat VCF product. Biomes were aggregated from the 36 land cover types defined in the original CCI map, with the two woodland savanna biomes separated using (a) (see Appendix A).

Figure 4.

Example region of interest (ROI) containing the fire shown in Figure 1 along with matchup active fire pixels (*white triangles*) from the Meteosat FRP-PIXEL product detected between midnight and the MODIS overpass time. (a) MAIAC 1km AOD and SEVIRI active fire (AF) pixels; (b) histogram thresholding to discriminate the plume from the surrounding ‘ambient’ background. (c) SEVIRI AF pixels detected within the convex hull of the plume are considered to come from the same ‘fire’ that produced the smoke plume. The fire radiative energy (FRE) of the causal fire is then calculated from these observations and used to match to the AOD-derived total particulate matter (TPM) (see Figure 5).

Figure 5.

Smoke emission coefficients (C_{biome}; in g.MJ^{-1}) for the six African fire-affected biomes defined in Section 4.1, each derived from the slope of an orthogonal distance regression (ODR) between data on fire-emitted total particulate matter (TPM) and matching fire radiative energy (FRE). Grey shaded area defines the 95% probability prediction interval of the ODR-derived slope. Each scatterplot is accompanied by an illustrative insert that depicts the typical landcover for the biome as seen in Google Earth (example locations are Closed Canopy Forest, 10.359° S, 19.086° E; Grassland 21.180° S, 19.560° E; Managed Land 10.495° N, 7.586° E; Low-Woodland Savanna 7.085° N, 27.095° E, High-Woodland Savanna 12.523° S, 23.323° E; Shrubland 23.055° N, 22.242° E).

Figure 6.

(a) FREMv2 smoke emission coefficient (C_e) mapped at 0.05˚; (b) the matching 1˚ FEER C_e product; and (c) the difference. In (c), FEER grid cells whose value was derived from gap-filling or which were calculated from less than 15 samples were removed (see Ichoku and Ellison

(2014) for full details). (d) Shows the spatial distribution of the fire matchups used to derive the FREMv2 C_{biome} values of Figure 5.

Figure 7.

Monthly total particulate matter (TPM) emissions from landscape fires for 2013 to 2018, as derived using the FREMv2 methodology *(blue)* applied to the Meteosat FRP-PIXEL product of Wooster et al. (2015). Corresponding monthly TPM emissions are shown from GFEDv4.1s *(green)*, GFASv1.2 *(purple)*, and the FEERv1.0 coefficients applied to the GFASv1.2 *(red)* and SEVIRI FRE data *(yellow)*.

Figure 8.

Total particulate matter (TPM) emission density (g.m^{-2}) across Africa for 2016 as determined by GFEDv4.1s (0.25° grid cells), GFASv1.2 (0.1° grid cells), FEERv1.0-GFASv1.2 (0.1° grid cells), FEERv1.0-SEVIRI (0.05° grid cells), and FREMv2 inventory derived herein (0.05° grid cells). The red 20° × 20° region outlined in the top left GFED plot is shown magnified for each inventory in the right-hand column.

Figure 9.

Mean monthly contribution (%) of fires to total particulate matter (TPM) emissions in each of the six FREMv2 biomes from 2013 to 2018 in (a) Northern Hemisphere Africa and (b) Southern Hemisphere Africa.

Figure 10.

Monthly total emissions (Tg) of (a) CO_2; (b) CO; and (c) CH_4 for African landscape fires as estimated by FREMv2 (*blue*) between 2013 and 2018. Corresponding values from GFEDv4.1s (*green*), GFASv1.2 (*purple*), FEERv1.0-GFASv1.2 (*red*) and FEERv1.0-SEVIRI (*yellow*) are shown for comparison.

Figure 11.

Fuel consumption per unit area (F_c, kg.m^{-2}) mapped at 0.25˚ from (a) 2016 FREMv2 dry matter consumed (DMC) totals and the FireCCISFD11-estimated burned area, and (b) GFEDv4.1s. (c) Per-biome FREMv2 F_c frequency distributions and derived means, medians and standard deviations. Note that F_c values in (a) apply only to the burned area patch inside a given pixel, and not the 0.25° pixel as a whole.

Appendix A - CCI landcover classes and VCF Tree cover % assigned to each FREMv2 biome.

Appendix B - Mean percentage contribution of different biomes to the fire radiative energy (FRE) released by fires between 2013 and 2018. On average woodland savanna fires contribute the greatest total FRE throughout the year, except for in November, and this means their determination is especially important for overall smoke emission estimate accuracy. The importance and abundance of fires in this biome is reflected in the high numbers of fire-plume matchups identified for both the *low- and high- woodland savanna* biomes (Figure 5).

Appendix C – Percentage difference in fuel consumption per unit area (F_c, kg.m^{-2}) calculated at a 0.25˚ resolution for 2016 African fires by FREMv2 (Figure 11a) and GFEDv4.1s (Figure 11b). The former provides significantly higher values in around half of the 0.25° grid cells. Figure 11c provides the per-biome F_c statistics coming from FREMv2.